Department of Physics and Astronomy
University of Heidelberg

Bachelor Thesis in Physics
submitted by

Marius Sparn

born in Heidelberg (Germany)

2017

Magnetic Fields for Cooling and Trapping of Potassium Atoms

This Bachelor Thesis has been carried out by Marius Sparn at the
Kirchhoff-Institute for Physics in Heidelberg
under the supervision of
Prof. Dr. Markus K. Oberthaler

Abstract

Magnetic Fields for Cooling and Trapping of Potassium Atoms

This thesis presents a versatile setup to precisely control magnetic fields for trapping and cooling of potassium atoms as well as the control of their interactions via a magnetic Feshbach resonance. It consists of an arrangement of water-cooled coils to generate high magnetic fields and field gradients, as well as a pair of coils for each spatial dimension to compensate extrinsic fields and to fine tune the applied field. Special emphasis is put on the uniformity of the field, since it determines the deviations of the scattering lengths within the trapping region. The field of the water-cooled coils is simulated taking into account their actual geometry and winding imperfections. The design and winding of the compensation coils is presented. Their resulting fields, inductances and resistances are characterized and compared to simulated results and analytical calculations. The agreement of measured and simulated results qualifies the use of the coils in the experiment and to predict the field configuration in the trapping region from numerical simulations.

Zusammenfassung

Magnetische Felder zum Kühlen und Speichern von Kaliumatomen

Diese Arbeit behandelt einen vielseitigen Aufbau zur präzisen Einstellung magnetischer Felder für das Kühlen und Speichern von Kaliumatomen und der Kontrolle deren Wechselwirkung mit Hilfe einer magnetischen Feshbach-Resonanz. Dieser besteht aus einer Anordnung wassergekühlter Spulen für die Erzeugung hoher Felder und Feldgradienten, sowie einem Spulenpaar pro Raumrichtung um äußere Felder zu kompensieren und das angelegte Feld fein abzustimmen. Besonderer Wert wird auf die Homogenität des Feldes gelegt, da diese die Abweichungen der Streulänge in der Fallenregion bestimmt. Die wassergekühlten Spulen werden unter Berücksichtigung ihrer echten Geometrie und Wicklungsunregelmäßigkeiten simuliert. Die Dimensionierung sowie der Wicklungsprozess der Kompensationsspulen wird dargestellt. Messungen der resultierenden Felder, Induktivitäten und Widerstände werden mit simulierten, sowie analytischen Werten verglichen. Die Übereinstimmung zwischen Messung und Simulation qualifiziert die Spulen für den Einsatz im Experiment, sowie die numerische Simulation für eine Vorhersage der Feldkonfiguration in der Fallenregion.

Contents

1 Introduction

As early as 1924 Albert Einstein noticed the relevance of Satyendra Nath Boses work on photon statistics for bosonic (integer spin) particles and postulated the so called Bose-Einstein condensate (BEC) as a new phase of matter [1],[2]. But is was not until 1995 that a BEC was obtained for clouds of trapped alkali-metals by the groups of Cornell and Wieman at JILA for ^{87}Rb [3] and Ketterle at MIT for ^{23}Na [4]. Today these condensates of trapped atoms are of particular interest for the field of bosonic quantum physics. Since Feshbach resonances can be used to tune the effective interaction potential of the particles, a variety of quantum systems can be mapped on the atoms of a condensate in suitable trapping potentials. The trapped bosons act like a quantum simulator of the model quantum system. The concept of a quantum simulator was first proposed by Feynman in 1982 [5] and can not only be used to explore the properties of specific quantum systems, but also to benchmark theories describing the behavior of many-particle systems.

The context of the work described here is an experiment to achieve a BEC-state of a cloud of atoms of the potassium isotope ^{39}K. This is enabled by a broad Feshbach resonance of the $|1,1\rangle$ hyperfine state at around $403.4\,\mathrm{G}$ [6], which allows tuning to repulsive interactions, a prerequisite for achieving sizable BECs. The large width of the resonance of $52\,\mathrm{G}$ allows for a precise tuning of the scattering length and therefore the effective interactions in the condensate.

This thesis focuses on the role of the magnetic field and its experimental control, needed not only to tune the scattering length but also for the different steps of the cooling processes in order to reach the BEC phase transition around $150\,\mathrm{nK}$ [7]. Following a short introduction of the experimental concepts and required theory in Chapter 2, Chapter 3 explores influences of asymmetries of the water-cooled coils, which produce a quadrupole field for magneto-optical as well as magnetic trapping and cooling as well as a homogeneous offset field for the tuning of the scattering length. Here, the approach was to simulate the field of the already manufactured coils to validate its suitability for the experiment, especially for the configuration needed to reach the vicinity of the Feshbach resonance. At this point a high uniformity of the field is crucial because otherwise the scattering length can differ significantly within the trapping region. Chapter 4 covers the compensation coils, which are needed to minimize the effects of any extrinsic magnetic fields, such as the earths magnetic field and magnetic fields arising from electrical equipment. Since the six coils, one pair compensating a single spatial dimension, were build during this work, the designing process of the coils is described. Measurements including resistance, inductance and the magnetic field are analyzed. The latter is compared to simulated results in order to verify the accuracy of the simulation, which was used in turn to predict influences of nonuniformities on the trapping region.

2 Experimental and Theoretical Background

2.1 Cooling and Trapping

The planned experimental cycle starts with laser-cooling in a two-dimensional magneto optical trap (2D-MOT), which pre-cools the atoms from the hot background vapor in a vacuum chamber. A push beam transfers the atoms into a 3D-MOT inside the science chamber, which is connected via a differential pumping tube. After sufficiently many atoms are captured in the 3D-MOT, cooling below the Doppler-temperature is achieved with a gray molasses stage [8]. This allows for further evaporative cooling in a magnetic trap. Finally the atoms are loaded into a dipole trap [9], where further evaporative cooling and the transition to a Bose-Einstein condensate is enabled by the use of a Feshbach resonance. The goal is not only to reach this phase, but also to retain as much atoms as possible for the experiments to be performed later on.

2.1.1 Magneto-Optical Trap

A magneto-optical trap uses the momentum of photons $\vec{p} = \hbar\vec{k}$ to confine the atoms in position and momentum space. To understand the basic principles we first consider a two level atomic system denoted by J=0 and J=1 with a transition energy $E_0 = \hbar\omega_0$ moving in a single spatial dimension. To confine the atoms in momentum space one sets up two counter-propagating laser-beams with a frequency ω which is slightly detuned below the transition frequency $\omega_0 = \omega + \delta$. Therefore the photon scattering rate is small for stationary or perpendicular moving atoms and more importantly equal for both directions. If however an atom moves in the direction of a laser beam with velocity $\vec{v}$ its effective frequency gets Doppler shifted by $\vec{k}\vec{v}$. In its comoving frame this corresponds to a blue-shift of one beam (the counterpropagating one in the laboratory frame) and a red-shift of the other one. This results in unequal scattering rates and the atom gets slowed down by the momentum transfer of the photons. After each scattering process the atoms fall back to the ground state J=0 via spontaneous emission. The corresponding photon gets emitted in a random direction. Therefore the corresponding momentum kicks average to zero for a lot of these processes. By setting up a pair of laser beams in each of the three spatial axes, one can confine the atoms in momentum space, which corresponds to cooling them down. This process is also called optical molasses.

For confinement in position space one can additionally add a magnetic field gradient typically on the order of $10\,\mathrm{G/cm}$. This gradient is produced by a pair of coils with opposite directions of current (in the later experiment these are the multicoils). These produce a quadrupole field with a point of vanishing field in the center. Due to the Zeeman effect, this magnetic field shifts

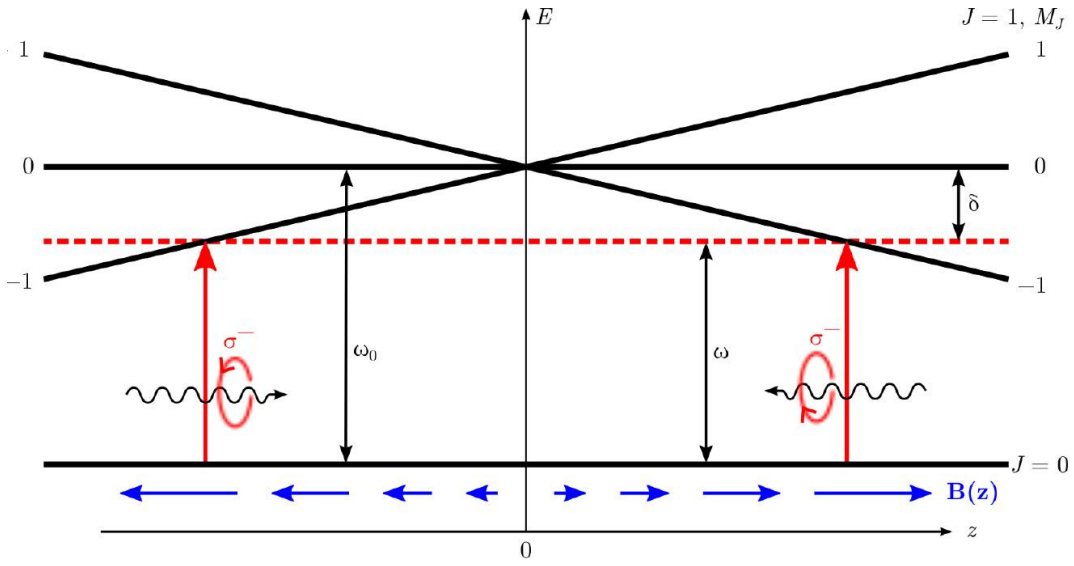

Figure 2.1 Schematic plot of the capturing process in the MOT for a two level atom. The counter-propagating laser beams are plotted at their point of resonance with a resting atom. Nevertheless do unequal scattering rates confine the atoms in position space not only at this point. Cooling of the atoms takes place, since their velocity corresponds to a frequency shift of the beams depending on their relative direction, resulting in unequal scatering rates, too. Fig. taken from [10] with adjusted labels for a quantization axis locally parallel to the magnetic field.

the energies of the sublevels $M_j = 1, 0, -1$ (see Fig. 2.1). Therefore for positions outside the center the $M_j = -1$ sublevel will be closer to resonance with the laser beams. According to the selection rules for the transition one has to adjust the polarity of the light to σ^-. By choosing the right polarity for the beams one can set this up such that atoms outside the center experience a restoring force towards the center. Note that due to the switch of sign of the magnetic field in the center, the relative polarity of the beams switches sides, while the energy splitting of the hyperfine states does not. Therefore the outgoing beam is off-resonant and on one axis one has to shine in light with equal polarities.

^{39}K is not a two level system like described above [11]. Nevertheless the basic principle and especially the magnetic field requirements remain the same. In the experiment two MOTs are used. The first one confines the atoms in only two spatial dimensions and is therefore called 2D-MOT. It is used to cool the thermal atoms that are dispensed by an oven. Since the atoms are only confined in two dimensions, they are distributed on a line. An additional beam aligned with that line, the so called push beam, transfers a small momentum to the atoms. This pushes the atoms through a differential pumping stage into the 3D-MOT region in the science chamber. In this way the actual MOT is loaded with a stream of already pre-cooled atoms and can also operate with much less thermal atoms around, which otherwise would severely limit the lifetime of the BEC. Since the cooling process in the MOT is limited to the Doppler temperature [12], which corresponds to 145 µK for ^{39}K [11], further cooling has to be achieved through other techniques. Common sub-Doppler cooling mechanisms (which for most species can be used inside the MOT) are highly inefficient due to the small hyperfine splitting of ^{39}K [13]. The next stage will therefore be a gray molasses stage, for which temperatures as low as 6 µK have been reported [8].

2.1.2 Magnetic Trap and Evaporative Cooling

In principle it is possible to load the dipole trap directly from the gray molasses [8], which renders the magnetic trap unnecessary. However, a lot of laser power is required to obtain deep optical traps with a big volume, such that a large fraction of the laser-cooled atoms can be captured. An option to obtain larger samples could therefore be to employ a magnetic trap as an intermediate step. A quadrupole trap is the easiest way of realizing this. The magnetic dipole moment $\vec{\mu}$ of an alkali atom in its ground state consists of the magnetic moment of the spin $\vec{S}$ of its valence electron and the spin $\vec{I}$ of its nucleus with their respective coefficients. Therefore the total energy in an external magnetic field sums to:

$$E = \frac{\mu_\mathrm{B}}{\hbar}(g_\mathrm{S}\vec{S} + g_\mathrm{I}\vec{I}) \cdot \vec{B} \tag{2.1}$$

Depending on the Zeeman-sublevel this can either result in an increase of energy or a decrease. Therefore the resulting force is either towards decreasing field, which is called low-field-seeker, or towards increasing field, a so called high-field-seeker. Since it is not possible to get a local maximum of the magnetic field one can only trap low-field-seekers (generalization of Earnshaws theorem [14]). Like in the MOT stage two coils with opposite directions of current produce a quadrupole field. This results in a local field minimum in their center and nearly constant magnetic field gradients. In a comparable experiment, which includes a magnetic trap for ^{39}K, a magnetic field gradient of $190\,\mathrm{G}$ for the z-direction and $90\,\mathrm{G}$ for the x- and y-direction was used [15]. To prevent losses by so called spin-flip Majorana transitions [16] in the zero field region in the center due to the small energy splittings of the hyperfine states, one can use an additional optical dipole trap, which shifts the trap center slightly out of the region of vanishing magnetic field.

The atoms trapped with this technique can then be evaporatively cooled. In thermal equilibrium the energy of the atoms is Boltzmann-distributed. From this we can depict the process of evaporative cooling via looking at discrete steps. First one lowers the effective depth of the magnetic trap until the atoms with the highest energies are able to escape (which is done with a technique called RF-knife). The remaining atoms will rethermalize via collisions, which means their energies will again form a Boltzmann distribution. The mean energy of the new distribution will be lower than before, since the atoms that left the trap in the last step had an energy way higher than the old mean energy. Via further lowering of the trap depth one can therefore lower the mean energies of the remaining atoms, which corresponds to cooling them down. This process works also for continuously lowering of the trap depth but one has to keep in mind that the time the system needs to rethermalize determines how fast this process can be done. If one reduces the barrier of the trap more slowly, less atoms are needed to escape for reaching the same final temperature, since due to a more perfect thermalization, escaping atoms posses optimum high energies. Instead other loss processes will dominate. One therefore has to make a trade-off. In principle cooling ^{39}K below the temperature of the BEC-transition should be possible using this technique, but would result in a collapse of the just obtained condensate due to attractive interactions [17]. To avoid this one has to load the atoms into a dipole trap above the BEC temperature. By operating two coils with unidirectional current flow, one can apply a magnetic fied suitable to tune the collision properties as briefly illustrated below. This allows for a further evaporation of atoms to reach below the transition temperature. According to [18] this process can be enhanced for a magnetic field of $395.2\,\mathrm{G}$, which corresponds to a

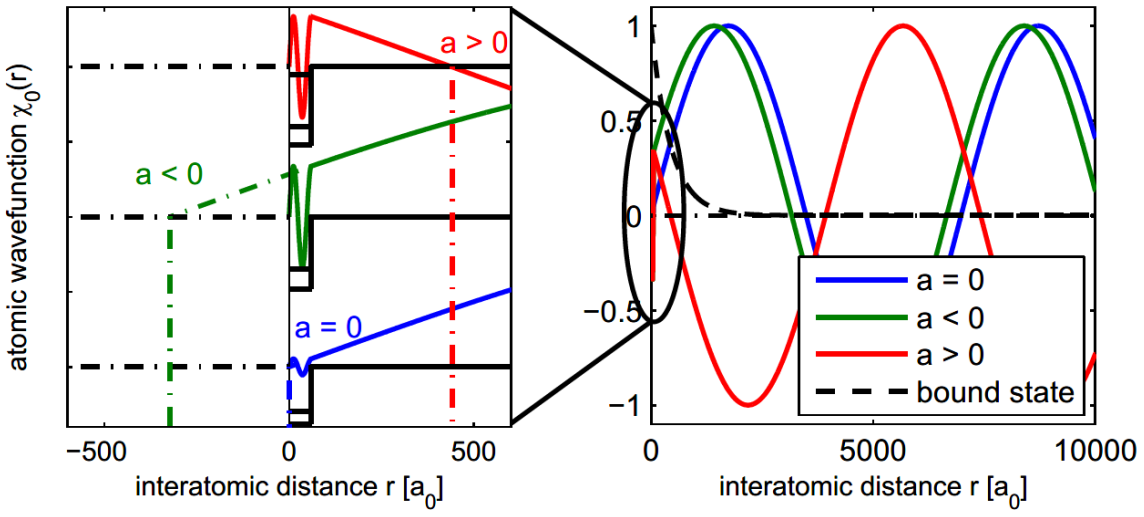

Figure 2.2 Plot of the atomic wavefunctions for different resulting scattering lengths a. For the microscopic scale of the potential (left), one can see the linear extrapolation of the wavefunction resulting in the intersection point defining a. The macroscopic scale of the wavefunction at high distances r from the scattering point (right) shows the phase difference between incoming and scattered wave, when the blue $a = 0$ wave is considered as being also the incoming wave (since $a = 0$ results in no phase difference, see Eq. 2.4). Fig. taken from [20].

scattering length of $a \approx 180\, a_0$. As one can see in the next section this increases the total cross section (Eq. 2.5) and therefore enhances the rethermalization process, which results in a higher efficiency of the evaporation.

2.2 Feshbach Resonance of ^{39}K

In the experiment a Feshbach resonance of the hyperfine state $|1, 1\rangle$ of ^{39}K located at (403.4 ± 0.7)G ([6]) will be used to tune the scattering length during the evaporation process and in the condensate. This section introduces the basic properties of the scattering length itself as well as the Feshbach resonance (additional information and basic derivation can be found in [19], that this summery is based on).

2.2.1 Scattering Length

The scattering length a is used to describe the interaction properties of particles with low kinetic energy (corresponding to small $k = |\vec{k}|$). For interatomic potentials which are spherically symmetric and short ranged ($< 1/r$) one can assume a scattering amplitude $f(\theta)$, which depends only on the angle θ between the relative momenta before and after scattering. The total wave function consists of the incoming wave and the scattered one:

$$\Psi = e^{ikz} + f(\theta)\frac{e^{ikr}}{r} \tag{2.2}$$

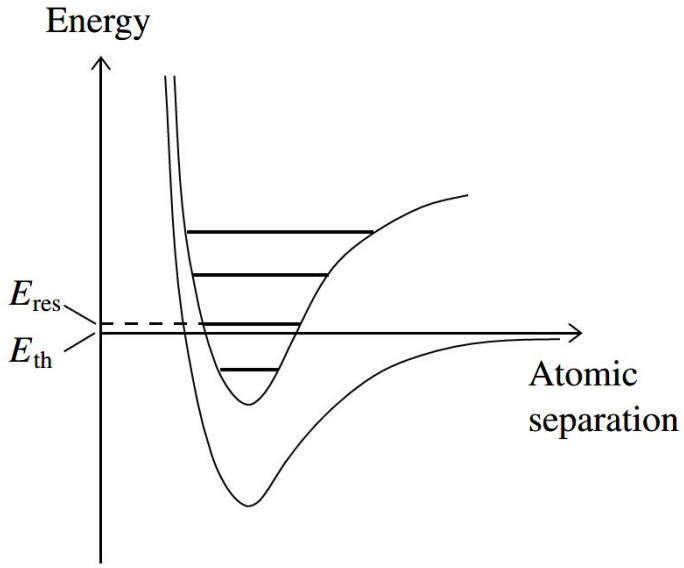

Figure 2.3 Schematic plot of the open and closed channel used for a Feshbach resonance. E_{res} is the energy of the bound state and E_{th} is the threshold energy of the open entrance channel. Fig. taken from [19]

Here the incoming direction was set to the z-direction, k is the wave number of the incoming wave and r is the distance to the scattering center. For low energies the wavelength is much larger than the short ranged scattering potential. Therefore any potential can be considered spherically symmetric and (since the energies are low) higher angular momenta do not contribute and it is sufficient to consider s-wave scattering only. For the asymptotic limit $f(\theta)$ approaches a constant, that yields the point of intersection of the extrapolated wave function with the z-axis, which is identified as the scattering length $a = -f(\theta)$:

$$\Psi = 1 - \frac{a}{r} \tag{2.3}$$

As one can see in Fig. 2.2 this intersection point corresponds to a phase difference δ on the macroscopic scales of the wave function:

$$\delta = -ka \tag{2.4}$$

In this picture one can understand that negative (positive) scattering lengths act like an attractive (repulsive) interaction. For scattering lengths close to zero the gas can be considered as noninteracting. The latter gets even clearer by looking at the resulting total cross section σ for identical bosons and s-wave scattering:

$$\sigma = 8\pi a^2 \tag{2.5}$$

2.2.2 Feshbach Resonance

Feshbach resonances arise for scattering particles, which share a bound state with a magnetic moment different from the one of the two incoming particles. While this bound state is part of

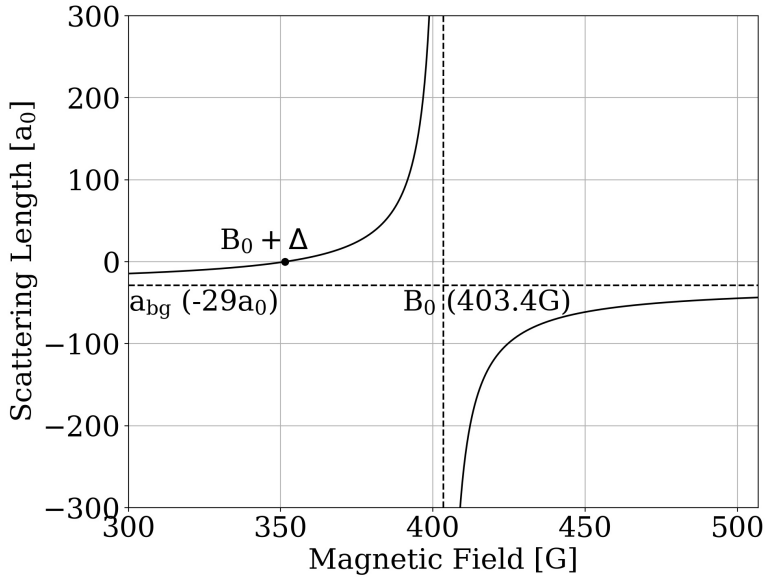

Figure 2.4 Dependence of the scattering length a in units of the Bohr radius a_0 on the magnetic field B in [G] for the $|1,1\rangle$ hyperfine state of ^{39}K in the vicinity of its Feshbach resonance located at (403.4 ± 0.7) G, with its width $\Delta = -52$ G and background scattering length $a_{\text{bg}} = -29\, a_0$ in units of a_0 (values taken from [6])

a closed channel and has a higher energy E_{res} than the energy of the incoming particles E_{th} (see Fig. 2.3), the difference in magnetic moment can be used to compensate for this the energy difference, via applying a magnetic field. In the vicinity of the resonance where $E_{\text{res}} - E_{\text{th}}$ is small, corresponding to $B \approx B_0$, the presence of the bound state affects the scattering length, as can be calculated via perturbation theory [19] and be approximated as:

$$a = a_{\text{bg}} \left(1 - \frac{\Delta}{B - B_0}\right), \tag{2.6}$$

with a_{bg} the background scattering length far off resonance and Δ being the width of the resonance, which corresponds to the difference in field between the field at resonance B_0 and the field at the zero crossing of the scattering length. For the $|1,1\rangle$ hyperfine state of ^{39}K, $\Delta = -52$ G and $a_{\text{bg}} = -29\, a_0$ ([6]), with a_0 being the Bohr radius, which leads to a dependence of the scattering length as plotted in Fig. 2.4.

2.3 Magnetic Properties of Circular and Square Coils

The scattering length shows an asymptotic behavior close to its resonance. Therefore to enable tuning over a large range one has to make sure that the magnetic field varies as little as possible within the trapping region. One could use a long solenoid, which has a practically constant magnetic field inside, and use magnetic shielding to block any undesired fields, such as the earths magnetic field and magnetic fields produced by electrical equipment. But as discussed before the setup also has to be able to produce magnetic quadrupole fields for the MOT and the magnetic trap. Also both the solenoid and the shielding would block any optical access

to the science chamber. This section covers the basic properties of circular and square coils, such as their magnetic field and inductance. Also the Helmholtz configuration will be derived for both shapes, which uses only two short coils to produce a uniform field in their center and therefore allows optical access.

2.3.1 Magnetic Field

The magnetic flux $d\vec{B}$ of a current I flowing at position $\vec{r'}$ can in general be calculated according to the Biot-Savart law:

$$d\vec{B}(\vec{r}) = \widetilde{\mu} I d\vec{l} \times \frac{\vec{r} - \vec{r'}}{|\vec{r} - \vec{r'}|^3} \tag{2.7}$$

with $\vec{r}$ being the point of interest, $d\vec{l}$ the differential element of the path of the current and the constant:

$$\widetilde{\mu} = 0.1\,\mathrm{G\,cm/A} \tag{2.8}$$

This is defined for practical reasons. Then all lengths are in centimeter and the resulting field B is in Gauss, while the current I can be plugged in in Ampere. From this one can calculate the field of a circular coil with N turns and radius R for its axis of symmetry (z-axis) in cylindrical coordinates:

$$\begin{aligned}
\vec{r} = \begin{pmatrix} 0 \\ 0 \\ z \end{pmatrix} = z\vec{e_z}\,, \vec{r'} = \begin{pmatrix} R\cos(\varphi) \\ R\sin(\varphi) \\ 0 \end{pmatrix} = R\vec{e_\rho} \implies d\vec{l} = \begin{pmatrix} -R\sin(\varphi) \\ R\cos(\varphi) \\ 0 \end{pmatrix} d\varphi = R\vec{e_\varphi} d\varphi \\
\vec{B}(z) = \widetilde{\mu} I N \int_0^{2\pi} d\varphi R\vec{e_\varphi} \times \frac{(z\vec{e_z} - R\vec{e_\rho})}{|z\vec{e_z} - R\vec{e_\rho}|^3} \\
= \widetilde{\mu} I N \int_0^{2\pi} d\varphi \frac{(R^2\vec{e_z} + Rz\vec{e_\rho})}{(R^2 + z^2)^{3/2}}
\end{aligned} \tag{2.9}$$

Integration over $\sin$ and $\cos$ from 0 to 2π is zero. Therefore only the z-component of the magnetic field is nonzero, which reflects the symmetry of the setup and yields the final result:

$$B(z) = \frac{2\widetilde{\mu}\pi I N R^2}{(R^2 + z^2)^{3/2}} \tag{2.10}$$

This calculation is also possible aside the axis of symmetry, but leads to elliptic integrals. Therefore a calculation without a computer is not practical and this work rather relies on a simulation, which respects the shape of the coils.

In principle this works the same for rectangular coils. Here one loop is parametrized as a set of four sides with length L and the axis of symmetry is chosen to be the x-axis (matching the experiment):

$$\vec{B}(x) = \widetilde{\mu} I N \int_{\text{-L/2}}^{\text{L/2}} dl \left(\frac{\begin{pmatrix}0\\1\\0\end{pmatrix} \times \begin{pmatrix}x\\-l\\L/2\end{pmatrix} + \begin{pmatrix}0\\0\\1\end{pmatrix} \times \begin{pmatrix}x\\-L/2\\-l\end{pmatrix}}{\left(x^2 + \left(\frac{L}{2}\right)^2 + l^2\right)^{3/2}} \right.$$

$$\left. + \frac{\begin{pmatrix}0\\-1\\0\end{pmatrix} \times \begin{pmatrix}x\\l\\-L/2\end{pmatrix} + \begin{pmatrix}0\\0\\-1\end{pmatrix} \times \begin{pmatrix}x\\L/2\\l\end{pmatrix}}{\left(x^2 + \left(\frac{L}{2}\right)^2 + l^2\right)^{3/2}} \right)$$

$$= \widetilde{\mu} I N \int_{\text{-L/2}}^{\text{L/2}} dl \frac{\begin{pmatrix}2L\\0\\0\end{pmatrix}}{\left(x^2 + \left(\frac{L}{2}\right)^2 + l^2\right)^{3/2}} \tag{2.11}$$

Again all components perpendicular to the axis of symmetry vanish. The final result is:

$$B(x) = \frac{2\widetilde{\mu} L^2 I N}{\left(x^2 + \left(\frac{L}{2}\right)^2\right) \cdot \left(x^2 + 2\left(\frac{L}{2}\right)^2\right)^{1/2}} \tag{2.12}$$

2.3.2 Helmholtz Configuration

The Helmholtz configuration is a way of setting up a pair of only two coils to reach maximum uniformity of the magnetic field in the center between the coils. This is done by choosing their distance d such that the second derivative of the field along their common axis vanishes. While this is not the biggest realizable uniform region [21], it has the highest uniformity in the center. Due to the symmetry of the setup, odd derivatives do not arise. This means in Helmholtz configuration the first nonzero derivative, while expanding around the center point, is $\partial^4 B/\partial x^4$, which leads to maximum uniformity. These constraints yield $d = R$ for radius R for circular coils. While sometimes this result is used to estimate $d = L/2$ for the sidelength L of rectangular coils, the actual result is $d = l/1.8365$ as shown below.

To proof the Helmholtz condition $d = R$ for circular coils, one adds the field of two coils (2.10) with distance $\pm d/2$ to the center point:

$$B(z) = 2\widetilde{\mu}\pi I N R^2 \left(\frac{1}{\left(R^2 + (z - d/2)^2\right)^{3/2}} + \frac{1}{\left(R^2 + (z + d/2)^2\right)^{3/2}} \right) \tag{2.13}$$

From this one can calculate the first derivative, which is zero due to symmetry for $z = 0$:

$$\frac{\partial B(z)}{\partial z} = 2\widetilde{\mu}\pi I N R^2 \left(\frac{-3(z - d/2)}{\left(R^2 + (z - d/2)^2\right)^{5/2}} + \frac{-3(z + d/2)}{\left(R^2 + (z + d/2)^2\right)^{5/2}} \right) \tag{2.14}$$

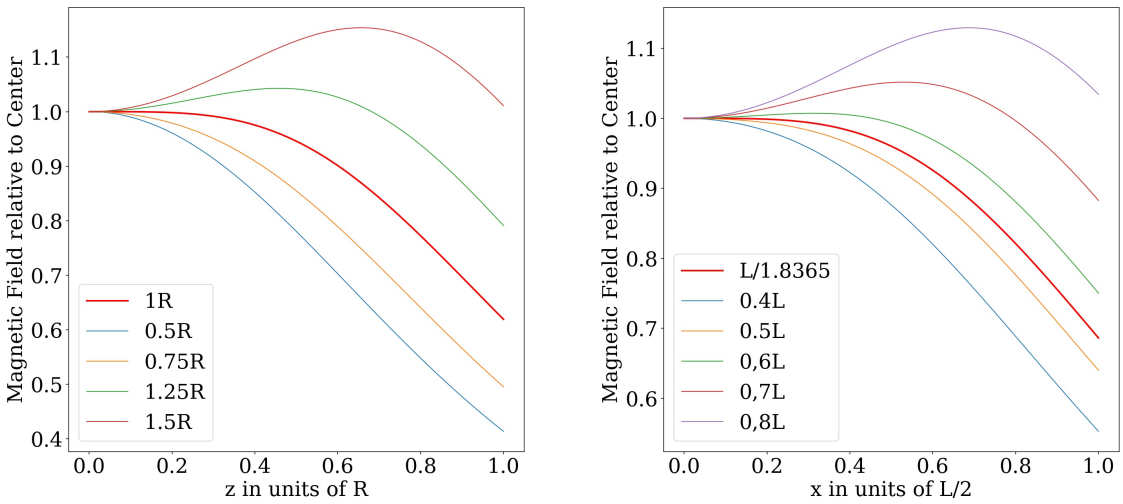

(a) (b)

Figure 2.5 Plot of the relative magnetic field of a pair of (a) circular and (b) square coils for different distances d and along their common axis. One can see that the Helmholtz distance (red) corresponds to the distance, where the maximum at the center (smaller d) turns into a local minimum (higher d), which is equivalent to the definition of the fourth derivative vanishing. In the case of the square coils one can see that, although $L/2$ is not far off, $L/1.8365$ leads to maximum uniformity at the center.

The second derivative yields the relation between R and d as discussed above:

$$\frac{\partial^2 B(z)}{\partial z^2} = 2\widetilde{\mu}\pi INR^2 \left(\frac{-3(R^2 + (z - d/2)^2) + 15(z - d/2)^2}{\left(R^2 + (z - d/2)^2\right)^{7/2}} + \frac{-3(R^2 + (z + d/2)^2) + 15(z + d/2)^2}{\left(R^2 + (z + d/2)^2\right)^{7/2}} \right)$$

$$\begin{aligned} \left.\frac{\partial^2 B(z)}{\partial z^2}\right|_{z=0} &= 2\widetilde{\mu}\pi INR^2 \cdot \frac{-6(R^2 + (d/2)^2) + 30(d/2)^2}{\left(R^2 + (d/2)^2\right)^{7/2}} \overset{!}{=} 0 \\ \implies & 30(d/2)^2 = 6(R^2 + (d/2)^2) \Leftrightarrow 4(d/2)^2 = R^2 \\ \implies & d = R \end{aligned} \tag{2.15}$$

Fig. 2.5 shows the relative magnetic field on the common axis of a pair of circular coils for different distances d. One can see that the Helmholtz distance is the transition point between a minimum and a maximum being at the center. This works similarly for rectangular coils:

$$B(x) = 2\widetilde{\mu}L^2IN\left(\frac{1}{\left((x+d/2)^2+\left(\frac{L}{2}\right)^2\right)\cdot\left((x+d/2)^2+2\left(\frac{L}{2}\right)^2\right)^{1/2}}\right.$$
$$\left.+\frac{1}{\left((x-d/2)^2+\left(\frac{L}{2}\right)^2\right)\cdot\left((x-d/2)^2+2\left(\frac{L}{2}\right)^2\right)^{1/2}}\right) \tag{2.16}$$

Since this yields extensive derivatives only the second one, evaluated at x$= 0$ is presented here (while the first one vanishes again at $x = 0$):

$$\begin{aligned}\left.\frac{\partial^2 B(x)}{\partial x^2}\right|_{\text{x=0}} &= 2\widetilde{\mu}L^2IN\cdot\frac{128(6d^6+18d^4L^2+11d^2L^4-5L^6)}{(d^2+L^2)^3(d^2+2L^2)^{5/2}}\overset{!}{=}0\\ &\Longrightarrow\ 6d^6+18d^4L^2+11d^2L^4-5L^6=0\\ &\Longrightarrow\ d\approx L/1.8365=0.5445\cdot L\end{aligned} \tag{2.17}$$

2.3.3 Inductance

The self-inductance L of a coil sets the relationship between changes in current I and induced voltage U to the coil:

$$U = L\frac{dI}{dt} \tag{2.18}$$

Depending on the definition of the directions of current and voltage, this equation is sometimes written with an additional minus sign, indicating that the induced voltage opposes the change in current (Lenz's law). The induced voltage will be relevant in the later setup, because it limits the rate of change of the magnetic field of the coils (shifting time). L itself can be calculated via:

$$L = \frac{\Psi}{I} \tag{2.19}$$

with Ψ being the magnetic flux linkage, which is equal to the number of turns N, times the magnetic flux Φ through the surface of one loop. Since Φ is proportional to I and N itself, L is constant with respect to I and proportional to N^2. For short coils the flux close to the wire is significantly higher than the one in the center. This does not only make the calculations difficult, but also leads to different mutual inductances between two loops depending on their relative positions in the coil. Therefore calculations of L are nontrivial and there exist a lot of different approximations, depending on the shape of the coil. To approximate the inductance of circular coils, Wheeler's formula is used in this work:

$$L = \frac{0.8a^2N^2}{6a+9b+10c} \tag{2.20}$$

with a being the mean radius, b the length and c the thickness of the coil. All lengths are given in inches ($1\,\text{cm} \approx 0.3937$ inches) and the result is given in microhenries. Whereas for square

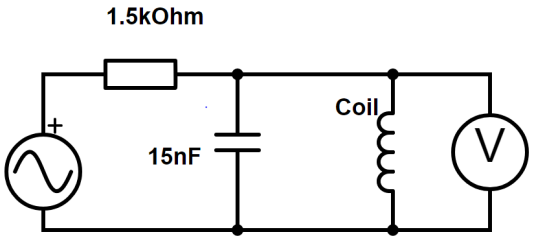

Figure 2.6 Schematic of the LC-Circuit. The circuit consists of a capacitor ($C = 15\,\text{nF}\ \pm 10\,\%$) in parallel connection with the coil to be measured and a resistor ($R = 1.5\,\text{k}\Omega$) in series connection. In the actual setup the current source (left) is a frequency generator and the voltage measurement (right) is done by an oscilloscope.

coils with sidelength l the following formula, which is attained via series expansion, is used [22]:

$$L = 0.008 l N^2 \left(\ln \frac{l}{b} + 0.72599 + \frac{b}{3l} - 0.007149 \frac{b^2}{l^2} + \mathcal{O}(b^4) \right) \tag{2.21}$$

Although this formula does not take into account the thickness of the coil, but places all loops within one line, it should be more accurate than not accounting for mutual inductances and therefore be sufficient for an approximation. To measure inductances an LC-circuit can be used. It consists of an additional capacitance C, which in the case of the built circuit is connected in parallel to the coil (Fig. 2.6). When driven with alternating current its effective resistance changes depending on the frequency (complex AC analysis can be looked up in [23]). This can be measured when a resistance R is in series connection. Then the coils (or equally the capacitors) potential difference rises, as one gets closer to the resonance frequency ω of the circuit.

$$\omega = \frac{1}{\sqrt{LC}} \implies L = \frac{1}{\omega^2 C} = \frac{1}{(2\pi f)^2 C} \tag{2.22}$$

3 Multicoils

The multicoils are water-cooled coils with a pancake geometry. They got produced by Oswald and are wound from a copper tube with a quadratic profile of $0.5\,\mathrm{cm}$. This allows for the cooling water to run directly through the coil. To isolate and fix the coils they are molded in transparent epoxy resin. Each coil consists of two layers with eight turns each (see Fig. 3.1). Two coils per side form the Helmholtz or quadrupole pair. The coils are mounted along the z-axis on brass posts (see Fig. 3.3), which were produced by the institutes workshop. These guarantee an inner distance of $5\,\mathrm{cm}$, which corresponds to $7.6\,\mathrm{cm}$ mean distance. This matches with the coils mean radius and is therefore the Helmholtz distance. In the experiment the coils serve multiple purposes. They produce the magnetic field gradient of in the MOT stage and for the magnetic trap. For the BEC in the dipole-trap the coils produce a uniform magnetic field in the regime of the Feshbach-resonance around $403\,\mathrm{G}$, to adjusts the scattering length. For the MOT configuration the upper and lower coils have to be operated with opposite currents for which anti-Helmholtz configuration (corresponding to $8.6\,\mathrm{cm}$ mean distance) would be ideal to get a constant magnetic field gradient. Nevertheless this should not affect the cooling process in the MOT too much, while a uniform magnetic field is crucial for experiments in the vicinity of a Feshbach resonance. As one can see in Fig. 3.1 the windings of the coil seem irregular. To some extend this is unavoidable since one has to realize the transition between the two layers, but its impact on the fields uniformity has to be examined. It was not possible to measure the magnetic field directly because the resolution of the measurement needs to be very high to see its impact on the trapping region, which is only about $100\,\mu\mathrm{m}$ wide in each direction. Thats why the coils fields got simulated to estimate the effects of the nonuniformities. Most simulations are done for xy-planes, parallel to the coils (which means the z-axis is their common axis). This allows to check for unanticipated asymmetries.

3.1 Simulation of the Magnetic Field

To simulate the magnetic field of the multicoils their shapes had to be estimated as exactly as possible. Therefore both sides of the coils got scanned in a flat bed scanner to have a high quality picture of both layers and minimized effects of parallaxes. These scans got digitalized with Engauge Digitizer [24], which also interpolates between the points set by hand. This gives around 1900 points per layer to work with. After setting up the coils in the simulation like they are in the experiment (see Fig. 3.2 and 3.3) the magnetic field is calculated with the Biot-Savart formula (Eq. 2.7) by making it a discrete sum over the vectors connecting the points (for the code see appendix A). The center of the field was first set to the plane at the midpoint between upper and lower layers, which should be exact due to the digitized layers being 2D and then optimized for a symmetric field in the center of the simulated region. This means in x- and y- direction the field point was set to the maximum of the field and in z-direction to the local

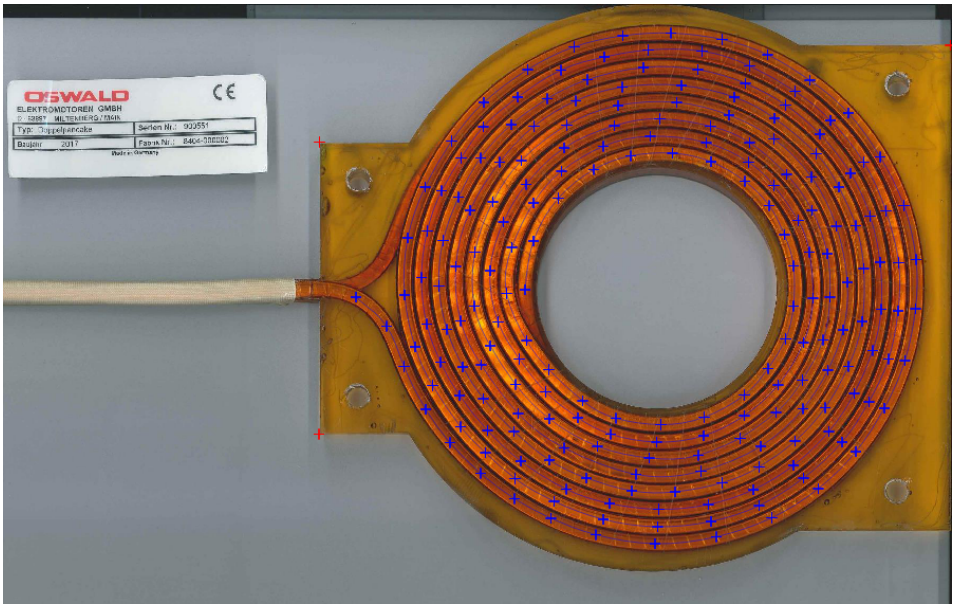

Figure 3.1 Example of a scan of one of the four multicoils. One can see the points set by hand on the tube of the coil and the interpolation done by Engauge Digitizer. This yields a total of about 1900 points per layer. A coordinate system is defined based on the edges of the epoxy resin (red crosses). The transition between the top and bottom layer is visible too. It is one of the reasons if not the main reason for asymmetries in the coils.

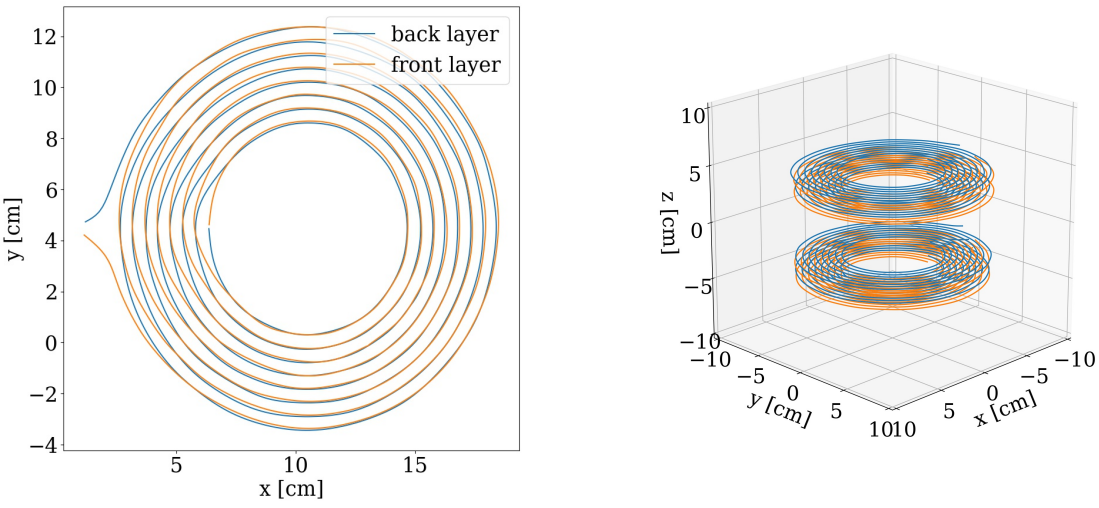

(a) (b)

Figure 3.2 (a) Single coil and (b) complete setup in the simulation. In (b) one can see that two coils are on top and two at the bottom, each consisting of two layers. This results in a total of eight layers, which are accounted for in each calculation within the simulation. While the coordinate plane in (a) is the coordinate system introduced while digitizing the coils (see Fig. 3.1), the one in (b) has its center point at the center of the Helmholtz configuration.

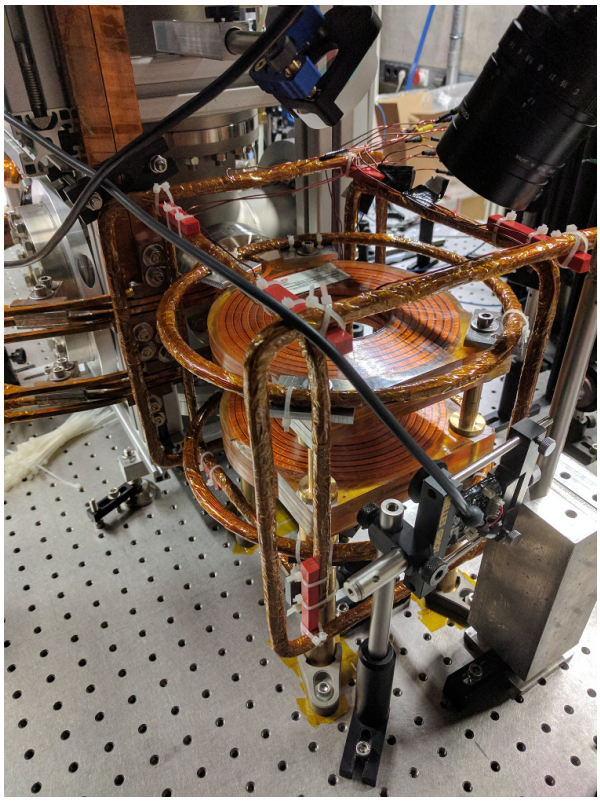

Figure 3.3 Picture of the completed coil setup in the experiment. One can see the four multicoils in the center, surrounded by the compensation coils. While the z-direction and coils (circular) are aligned with the multicoils, the x- and y- coils and their respective direction can be distinguished via the larger size of the x-coils. In the top left corner one can see the supply lines of the multicoils, consisting of four solid copper rods, which allow the individual drive of the top and bottom coils.

minimum, which in theory defines the center in all spatial directions. The fact that a local minimum was found means that the coils are not mounted in their actual Helmholtz distance (compare to Fig. 2.5), which differs from the one of the mean values due to the coils large extensiveness. While one could argue that this approach of centering levels out some of the asymmetries, this is the proper way for predicting influences on the experiments, since after all optimizing is done, the trapping region should be in the vicinity of this point. The simulation revealed that the center is about $210\,\mu\mathrm{m}$ shifted towards the upper coils in z-direction, which can only be explained by asymmetries. This should be no issue for the experiments since this is still well within the science chamber. What could be an issue, is the fact that the center point of the quadrupole configuration for the magnetic trap was found to be off by $-389\,\mu\mathrm{m}$ in x-, $149\,\mu\mathrm{m}$ in y- and $-232\,\mu\mathrm{m}$ in z-direction with respect to the Helmholtz-configuration. The total distance is therefore about $475\,\mu\mathrm{m}$, which has to be either compensated before the transition from magnetic (or hybrid) to pure dipole trap takes place, or the resulting nonuniformities have to be accounted for (and can be approximated via Figs. 3.5 and 3.6).

3.2 Resulting Properties

Fig. 3.4 shows the z-component of the field relative to the one at the center point in the xy-plane in the trapping region. The overall picture does not change significantly for the edges of the trapping region in z-direction. Nevertheless the rise in magnetic field for the edges shows that the coils are mounted at a larger distance than their Helmholtz distance (see Fig. 2.5). The magnitude of the magnetic field of about $4.06\,\mathrm{G/A}$ is enough for all planned applications, since the maximum current of the coils is in the range of $400\,\mathrm{A}$. The relative nonuniformity in the relevant region is not more than $4.2 \cdot 10^{-7}$ within one layer and smaller than 10^{-6} for the trapping region as a whole. In the vicinity of the Feshbach resonance located at $(403.4 \pm 0.7)\,\mathrm{G}$, which corresponds to a current of about $99.4\,\mathrm{A}$ this would correspond to a deviation of about $0.4\,\mathrm{mG}$. For the total width of $-52\,\mathrm{G}$ this is enough for simultaneous tuning of the scattering length in the whole trapping region, even close to the resonance (for an approximation of the errors of the scattering length see Fig. 3.6). One has to keep in mind that the accuracy of the total value of the field is not known, which means in the later experiment one has to determine the position of the resonance in terms of corresponding current, although one can be quite confident to find it near $100\,\mathrm{A}$. Theoretically the x- and y-component should vanish in the center point and therefore be negligibly small for the trapping region as a whole. The total value of the perpendicular component relative to the z-direction is indeed smaller than $3 \cdot 10^{-4}$, which corresponds to $4.5 \cdot 10^{-8}$ in terms of relative contribution to the total field. Although this is a clear sign for asymmetries in the coils, the resulting effects should be negligibly small. Besides the tiny effect on the norm of the field the transverse field component would also correspond to a tilt of the field of less than $0.02°$. Since perfect alignment of the dipole trap and the center of the magnetic field might be not possible, in Fig. 3.5 the deviation of the absolute field relative to the one at the center and its gradient for an extended region of $\pm 5\,\mathrm{mm}$ around the center in x- and y-direction are plotted. This can be used to approximate differences in total field, which are smaller than $4 \cdot 10^{-3}$ and can be compensated via adjusting the current. Additionally from the total value of the gradient, which is given in units of $1/100\,\mu\mathrm{m}^{-1}$, one can estimate the nonuniformity of the absolute field within the trapping region by multiplying

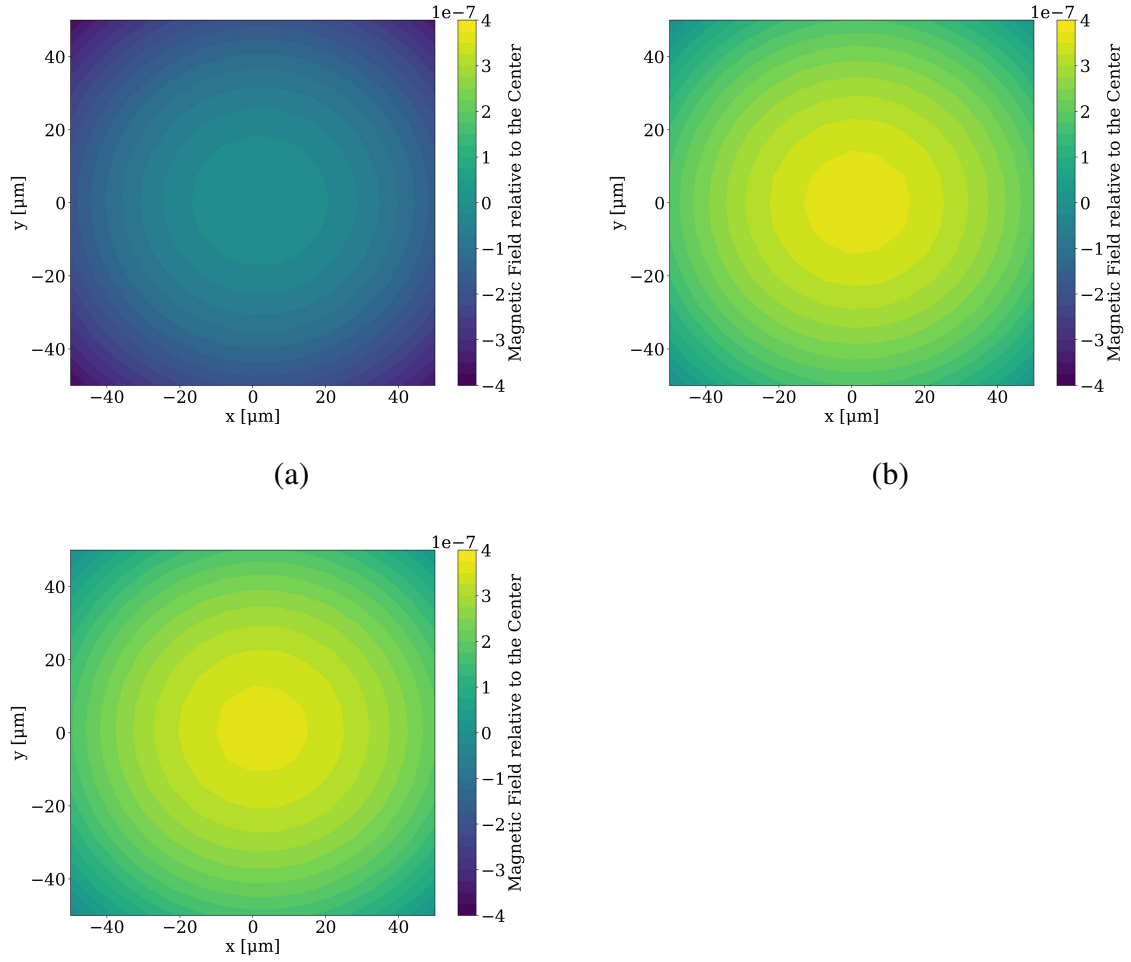

Figure 3.4 Z-component of the field in Helmholtz configuration relative to the center in the xy-plane at (a) $z = 0$, (b) $z = 50\,\mu\mathrm{m}$ and (c) $z = -50\,\mu\mathrm{m}$, which corresponds to the edges of the anticipated trapping region. One can see that the center point is a maximum in x- and y- direction and a (local) minimum in z-direction. This shows that the coils are mounted at a larger distance than their corresponding Helmholtz distance (compare to Fig. 2.5). All deviations between any two points in the region are smaller than 10^{-6}.

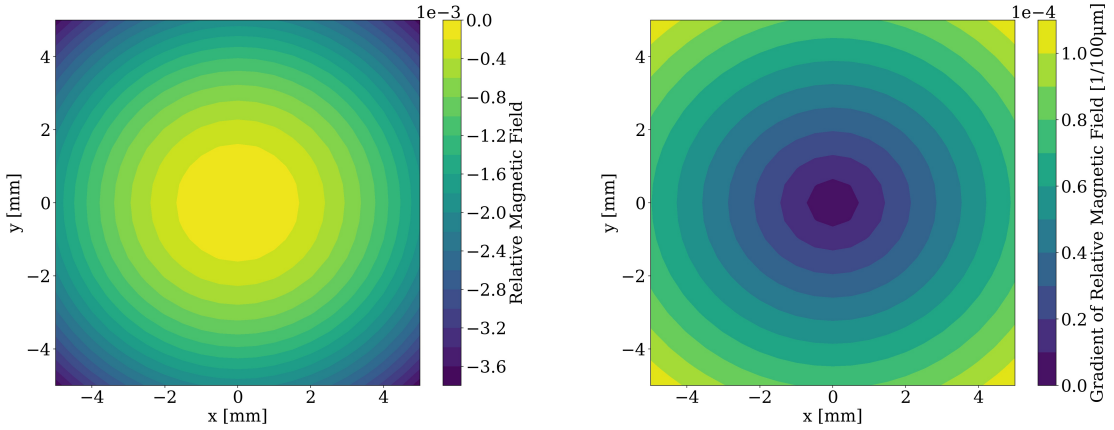

(a) (b)

Figure 3.5 (a) Relative deviation from the absolute field in the center and (b) total value of the gradient of the absolute field relative to the center in $1/100\,\mu\mathrm{m}^{-1}$ for an extended region of $5\,\mathrm{mm}$ around the center and the coils operating in Helmholtz configuration. One can see that the field in y-direction decreases slightly faster in both plots. This is a sign for the the wire elements parallel to x having a slightly bigger part in the generation of the field. While the magnitude in (a) has no units, the units in (b) are chosen in a way, that fast approximations of the uniformity within the trapping region are possible. Since the region extends about $100\,\mu\mathrm{m}$ to each side, one only has to multiply the value at a given position with the field, to get the deviation of the field.

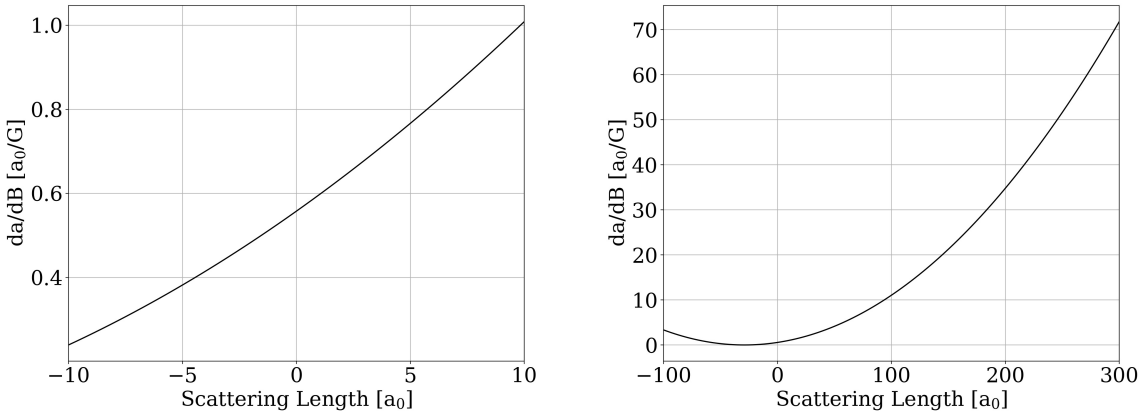

(a) (b)

Figure 3.6 Derivative of the scattering length a with respect to the magnetic field B for the Feshbach resonance located at $403.4\,\mathrm{G}$ for (a) the vicinity of the zero crossing and (b) a wide range of the scattering length. This can be used to approximate errors of the scattering length induced by errors of the field when multiplied with the fields error. Note that this approximation gets worse for big errors of the field, because the slope within the range of the error can not be approximated as constant in this case. This is particularly important near the resonance corresponding to large absolute a.

with the needed magnetic field for the desired scattering length. For example for the maximum gradient of about $10^{-4}{\cdot}1/100\,\mu\mathrm{m}^{-1}$ and a scattering length of $100\,a_0$ this would correspond to an error of about $0.4\,a_0$.

For opposite directions of current in the top and bottom coils, which is their quadrupole configuration for the MOT and the magnetic trap, the magnetic field gradients in Tab. 3.1 were found.

	x-direction	y-direction	z-direction
normalized magnetic field gradient $\left[\frac{\mathrm{G}}{\mathrm{A\,cm}}\right]$	0.449	0.471	0.920
desired gradient [G/cm]	95	95	190
corresponding current [A]	212	202	207

Table 3.1 Magnetic field gradients of the multicoils in quadrupole configuration (aquired via simulation) compared to gradients taken from [15] and their corresponding currents. The deviation of the gradients in x- and y-direction is due to the asymmetries of the coils.

Deviations within the gradient of one direction were about two orders of magnitude smaller than the last digit given in Tab. 3.1. Nevertheless the deviations in current needed for the desired gradient show the discrepancy of the actual coils and ideal ones, especially for the x- and y-component, which should be equivalent both in field gradient and current. Noticeable is the fact that the currents for the x- and y- direction differ from the one for the z-direction by the same amount, but opposite signs (accordingly their mean gradient is equal to half the gradient of the z-direction). This is a clear sign for asymmetries in x- and y-direction on the order of $\pm 2.5\,\%$ and is consistent with the faster drop in field in y-direction in the Helmholtz configuration (see Fig. 3.5). These asymmetries arise due to the connecting wires and transition between the layers being in regions of the coil parallel to the y-direction and therefore mostly weakening the x-direction (see Fig. 3.2). Especially the transition weakens the x-direction, since it is close to the center but consists of one wire only instead of two (one per layer). In addition to the transition itself, its presence also deforms the outer windings of the coil. Asymmetries of the quadrupole configuration should however not lead to problems, since neither for the MOT nor the magnetic trap a high uniformity is needed. Slightly different shapes of the trapping potential should not make a notable difference.

4 Compensation Coils

The compensation coils are used to deal with any undesired magnetic fields in the trap, such as the earths magnetic field and magnetic fields produced by electrical equipment. To be able to cancel field-components in all three spatial dimensions, a pair of coils is set up for each axis (see Fig. 4.1). For a uniform field in the center the coils should be set up in Helmholtz-configuration. As one can see in Fig. 3.3 this was possible for the z-coils only, since the mounts of the multicoils and the paths of the MOT-beams limit the realizable geometries.

4.1 Design and Construction

Since already the earths magnetic field of $\approx 0.5\,\mathrm{G}$ is within the range of $1\,\mathrm{G}$, the compensation coils should be able to even out at least $1\,\mathrm{G}$ in their center. Due to limited space the dimensions have been set such that the coils do not interfere with other equipment or the laser beams (see Tab. 4.1). Also the diameter of the copper wire was chosen to be $1\,\mathrm{mm}$, since tests with a diameter of $0.5\mathrm{mm}$ showed a relatively high heat development. This led to the number of turns per coil N and the applied voltage U being the only degrees of freedom left as explained below. On the one hand a low number of turns yields a low inductance L and is therefore desirable, to keep shifting times short and avoid high mutual inductances with the multicoils. On the other hand the coils should run at low power to keep ohmic heating at a minimum. The available home-built voltage controlled current source has 3 outlets with an upper limit of $1\,\mathrm{A}$ at $12\,\mathrm{V}$. Each pair is connected in series to guarantee equal current. This means every pair has a maximum power of $12\,\mathrm{W}$.

From Eq. 2.10 one can calculate a factor NI, for the z-coils to produce $1\,\mathrm{G}$ in their center:

$$\frac{NI}{B} = \frac{(R^2 + (d/2)^2)^{3/2}}{4\widetilde{\mu}\pi R^2} = 12.79\,\mathrm{A/G} \tag{4.1}$$

So the number of turns in one coil N times current I has to be adjustable to this value. Since the current is limited to $1\mathrm{A}$ in the planned setup, this means every z-coil has to have at least 13

	x-coil	y-coil	z-coil
shape	square	square	circle
mean sidelength/diameter [mm]	235	203	230
mean Helmholtz distance [mm]	128	110	115
mean planned distance [mm]	220	160	115

Table 4.1 Dimensions of the compensation coils. Only the mean values are given, since they are the relevant variable for most approximations. The corresponding inner sidelength/diameter is 1 cm smaller.

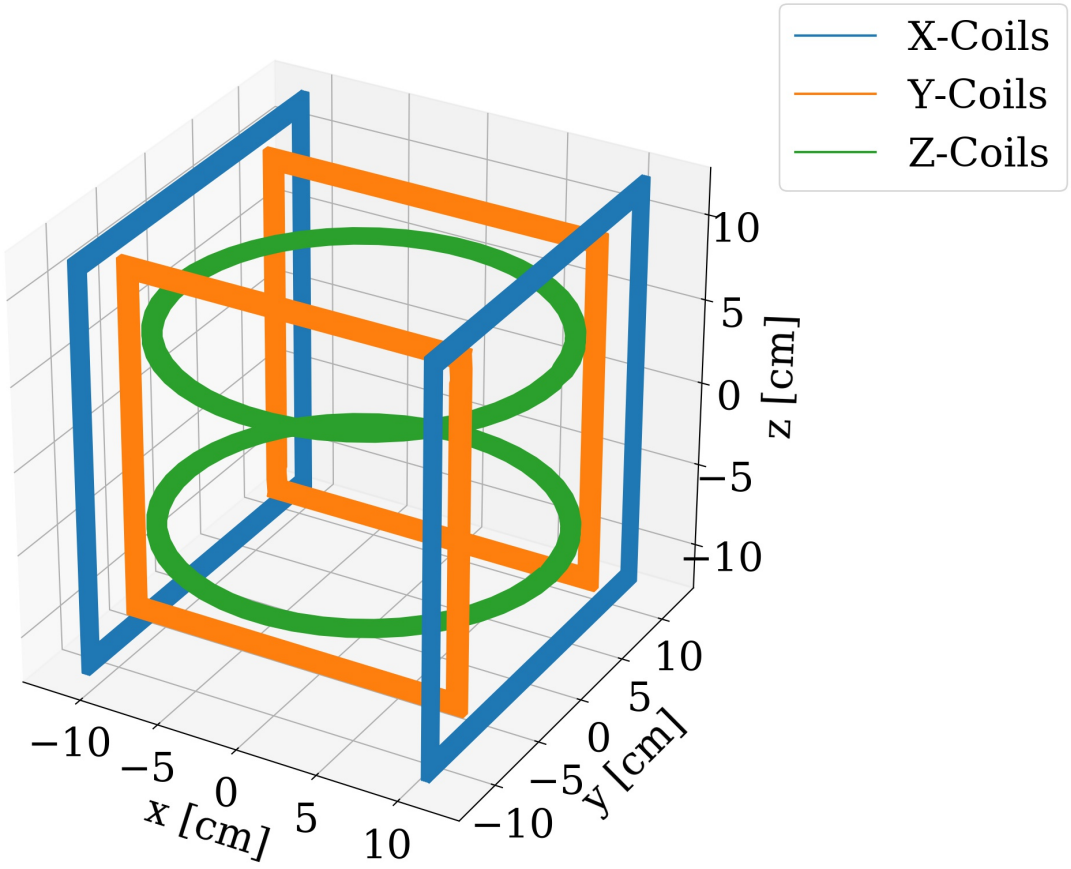

Figure 4.1 Compensation coils in the simulation. Positions and dimensions of the coils got modeled like in the experiment, meaning each coil consists of five layers and ten turns making a total of $N = 50$ turns. One can see that each pair of coils is named after the direction of their common axis, which is also the direction in which they compensate undesired fields.

turns. The resistance of copper is about $17.1\,\mathrm{n\Omega\,m}$, which leads to a resistance of the wire of $21.77\,\mathrm{m\Omega\,m^{-1}}$. Therefore the resistance R/N of a single turn is $15.73\,\mathrm{m\Omega}$. This determines the voltage U needed per Gauss, since the overall resistance is proportional to N, while I is inversely proportional to N for a given field. A factor two is needed to include the series connection of the coils:

$$\frac{U}{B} = \frac{NI}{B}\frac{2R}{N} = 402.2\,\mathrm{mV/G} \tag{4.2}$$

This shows technically 13 turns per coil would be enough, to reach 1 G in z-direction. But from the voltage one can see that the power supply can easily drive more turns, which was therefore used to extend the range of the field, by making 50 turns per coil.

The same can be done for square coils by using Eq. 2.12.

	x-coil	y-coil	z-coil
NI/B [A/G]	23.37	16.65	12.79
R/N [mΩ]	20.47	17.68	15.73
U/B [mV/G]	956.8	588.7	402.2

Table 4.2 Theoretical properties of the compensation coils. Note that the actual values differ. For the highest accuracy for total current per field NI/B and voltage per field U/B see table 4.8, for the resistance R table 4.3.

Based on Tab. 4.2 the x- and y-coils got also 50 turns, to extend their compensation ranges as well. Note that the voltage per Gauss factor U/B while being useful in the experiment for a first estimation of the voltage, depends on the actual resistance of the coils (Tab. 4.3) and their feed cables.

Coil Winding

For the actual winding of the compensation coils, different methods were applied, depending on the coils shape. For the circular coils a form, which was made by the institutes workshop, was used (see Fig. 4.2). This guaranteed not only the round shape, but also held the wire in place to limit the length of the coil. The square coils were only held on the edges, therefore the resulting length is not limited at the sides. This resulted in a rounder shape of the wire bundle at the sides. All coils are bundled with Kapton tape, which tightens their shape.

4.2 Experimental Results

To check the actual properties of the coils a series of measurements has been carried out. In this section results for resistance, inductance and the magnetic field both in plane of the coils and along the common axis of the pairs are presented.

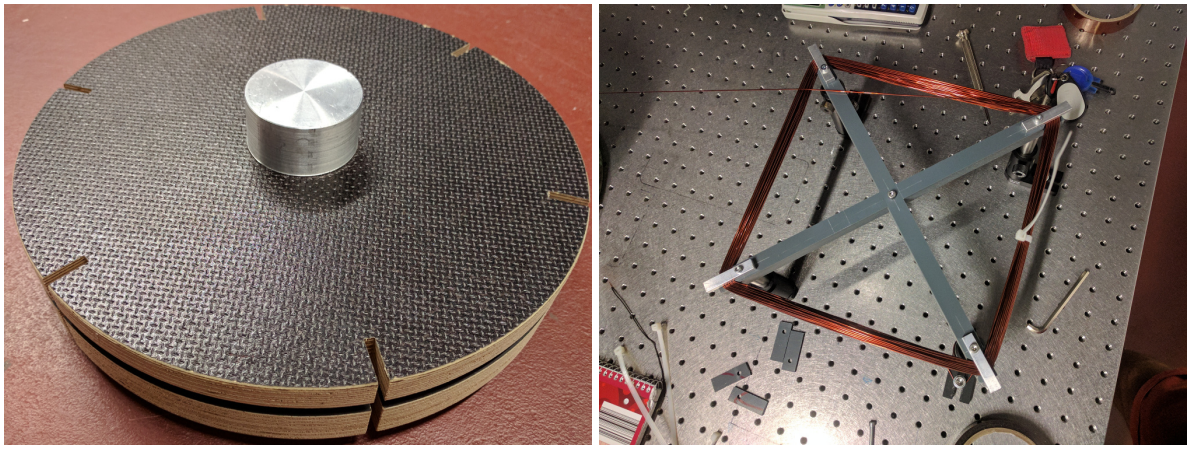

Figure 4.2 Form for circular coils, which can be mounted on a lathe, and the winding process of a square coil. The form guarantees a round shape and limits the length of the resulting circular coil. It also offers notches for zip ties. In this way the coil does not loose its shape between winding and bundling. In the case of the square coil, only the edges were held in place by a form. This led to slightly loose wire parts at the sides.

4.2.1 Resistance

The voltage drop of the coils was measured for six different currents in the range of 0.25 A to 3 A. Since this did not make a difference as one would expect, the mean results can be found in Tab. 4.3.

	x-coil 1 / 2	y-coil 1 / 2	z-coil 1 / 2
R_{theo} [mΩ]	1023.5	884	786.5
R_{exp} [mΩ]	$1087 \pm 12/1080 \pm 12$	$940 \pm 12/938 \pm 12$	$855 \pm 11/856 \pm 12$
(U/B) [mV/G]	1013 ± 8	625 ± 6	438 ± 4

Table 4.3 Resistance of the compensation coils. From the experimental values of coil 1 and 2 a new U/B factor was derived for each direction. For the final and most exact results see table 4.8.

The theoretical values did not take feed cables and transverse components of the windings into account. Therefore the experimental resistances are significantly higher. From those and the analytical (IN/B) factor a new (U/B) factor was derived.

4.2.2 Inductance

According to Eq. 2.21 and 2.20 one can approximate the inductances (see Tab. 4.4). For the square coils $b = 1$ cm was assumed and for the circular coils $c = 1$ cm and $b = 0.5$ cm, since the circular coils were wound on a form, which limited the resulting length to this value. To gain a better feeling for the approximation of the coils, that have slightly changing thickness and length within the loop, c and b got doubled for a second calculation (while radius and sidelength remained the same). The results influenced the dimensioning of the LC-circuit, since the resulting resonance frequency (see Eq. 2.22) should be in the lower kilohertz range to

fit to the frequency generator as well as the oscilloscope. There were no significant differences in the resonance frequencies of two coils of the same pair. Therefore only the mean values are presented (see Tab. 4.4).

	x-coil	y-coil	z-coil
L_{theo1} [mH]	1.83	1.52	1.25
L_{theo2} [mH]	1.51	1.25	1.06
resonance frequency f [kHz]	33.2	36.6	37.3
L_{exp} [mH]	1.53 ± 0.15	1.26 ± 0.13	1.21 ± 0.12

Table 4.4 Inductance of the compensation coils. The first theoretical value corresponds to the approximated dimensions of the coils, whereas the second one consists of doubled length b (and thickness c in the case of the circular coils), but unchanged sidelength and radius. While the second one fits well to the experimental values of the square coils, its merely a matter of demonstrating the influence of the shape on the inductance. The errors of the experimentally obtained inductances consist entirely of the $10\,\%$ error of the capacitance C, since all other uncertainties are negligibly small relative to that.

From this one can approximate the maximum induced voltage U_{max} (Eq. 2.18), for changes to the current I. One can assume that a field of $1\,\text{G}$ in the center of one of the pair of coils shall be switched off within $\tau = 0.5\,\text{ms}$. Assuming an exponential decay in current and the process to be complete when the field has dropped under $5\,\%$ ($\approx e^{-3}$) this yields:

$$U_{\text{max}} = -\frac{3I(2L)}{\tau} \tag{4.3}$$

The $2L$ in brackets denote that the inductance of both coils connected in series is added. This does not account for mutual inductances.

	x-coil	y-coil	z-coil
I [A]	0.453	0.332	0.256
U_{max} [V]	-8.3 ± 0.8	-4.9 ± 0.5	-3.7 ± 0.4

Table 4.5 Approximation for the induced voltage U for ramping down a field of $1\,\text{G}$ in the center of the field within $0.5\,\text{ms}$ below $5\,\%$ of the initial value. The induced voltages are on a manageable level, even for an order of magnitude faster switching. The current per Gauss ratio is taken from table 4.8

4.2.3 Magnetic Field

The coils were mounted at the distances they have in the experiment (see Tab. 4.1) and the field along their common axes was measured (picture 4.3). In Fig. 4.4 the results are compared to analytical ones based on Eq. 2.13 and Eq. 2.16 (as well as to the results of the numerical simulation). While the analytical results describe the general shape quite nicely, there is still a significant difference in the relative values. This can not be explained by positional offsets of the probe only. The probe (Bartington Mag03-IE-1000) measures with very high precision, so its error is negligible here. As one can see by looking at the results of the simulation (which is explained in detail below), it does make a difference, that the analytical formula does not

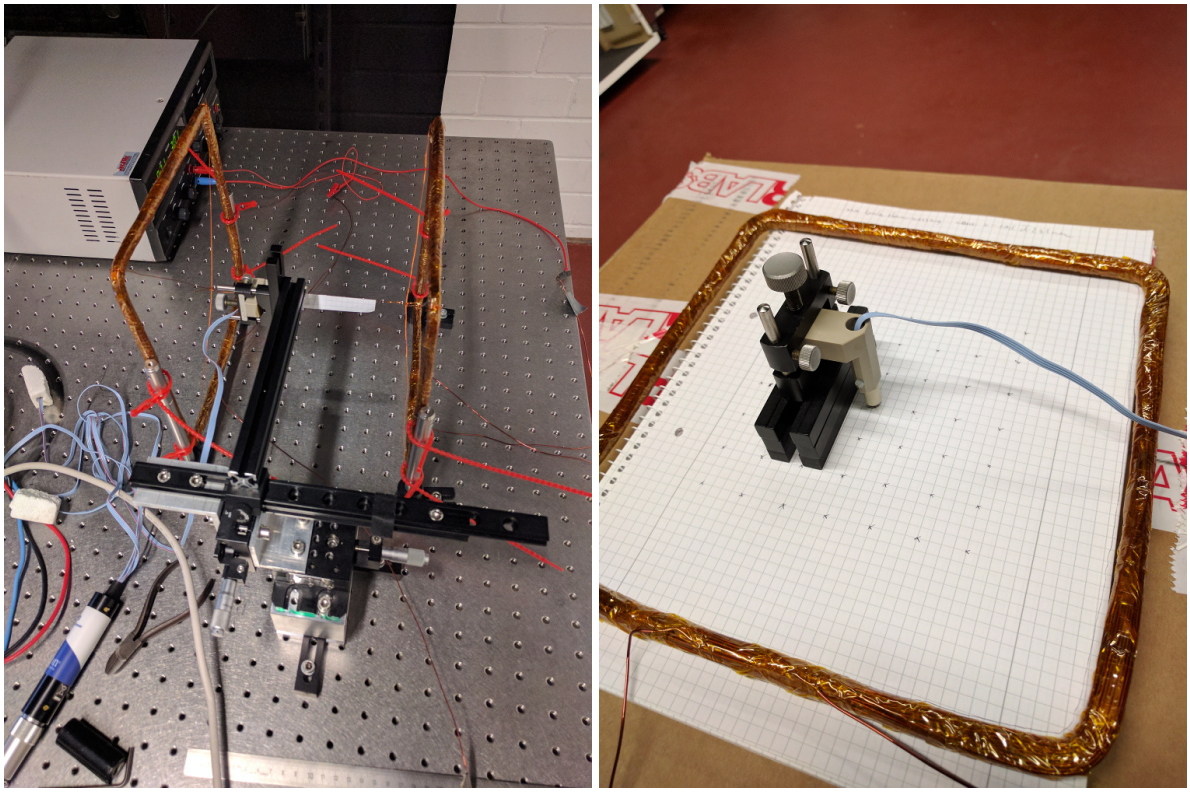

Figure 4.3 Experimental setup to measure the magnetic field along the coils common axis and in plane. Since the optical table alters the measurements in plane as one would expect, these measurements were done on top of a cardboard box.

take the shape of the coils into account. This can be understood based on Eq. 2.10 and Eq. 2.12, which makes clear that the field neither has a linear relation to the distance nor is it antisymmetric around the mean distance in any other way.

The field of the individual coils got also measured in plane (see Fig. 4.3) at a current of 2 A. This was done for both coils of each of the three axes, but since there are no significant differences between the identical coils the mean values are presented here in Fig. 4.6, where their relative values are compared to the simulated ones. From Eq. 2.10 and Eq. 2.12 one can calculate the fields normal component in the center of the planes (see Tab. 4.6). Except for the y-Coils, this fits very well to the experimental results (see Tab. 4.6).

	x-coil 1 / 2	y-coil 1 / 2	z-coil 1 / 2
B_{theo} [G]	4.81	5.57	5.46
B_{exp} [G]	$4.79/4.80 \pm 0.02$	$5.40/5.45 \pm 0.03$	$5.47/5.44 \pm 0.03$

Table 4.6 Theoretical and measured field of the compensation coils in the center of their plane for $I = 2\,\text{A}$

4.3 Simulation and Derived Properties in the Trapping Region

Since it is not possible to measure the magnetic field produced by the coils directly in the trapping region, one needs to simulate the coils. This does not only allow to check for deviations from expected behavior on the large scales, but one can also extend the simulation to the extremely small scales of the trap. The simulation works similar to the one for the multicoils. The magnetic field is calculated by discretization of the Biot-Savart law, Eq. 2.7. This time the coils did not get scanned in and digitalized because of the thin wire and the number of layers. Instead their windings got parametrized (including positional offsets between the turns due to the diameter of the wire) with a certain resolution per turn as a set of points.

4.3.1 Large Scales

At first the simulation was used to simulate the field along the coil axis for the distance the coils will have in the final setup (see Figs. 4.1 and 3.3). As one can see in Fig. 4.4 the simulated results reproduce the experimental ones slightly better than the analytical ones. There is arguably an offset left, but since the simulation takes the shape into account it is smaller than the one of the analytical results, especially for the square coils. Most likely some magnetic susceptibilities in the mount of the probe (Fig. 4.3) led to this remaining offset. This means the offset is of relative nature and one can account for that by adjusting the currents (which corresponds to normalizing all results to their respective center points, which can be seen in Fig. 4.5). Additionally the y- direction of the y-coils and the respective one of the z-coils has been adjusted (by $-2\,\mathrm{mm}$ and $5\,\mathrm{mm}$), to match to the other results. Especially for the y-coils the improvement between theory and simulation gets clear. All in all the simulated results resemble the experimental ones quite good in terms of shape. This is good since in the end it is merely a matter of uniformity of the field and not of its total value, since these can be adjusted via the current.

The measurements in plane can also be simulated. In Fig. 4.6, the results are compared to the measurements. While the shapes of simulations and measurements are similar and the measured field values fit both to the analytical as well as to the simulated fields in the center point (see Tab. 4.7), the measured values are significantly lower for the edges of the region. This difference can be explained by the probe being slightly out of plane, which is to some extend inevitable since the sensitive region of the probe is not pointlike. This leads to a higher distance from the wire and since the components get summed up quadratically to get the distance, the effect gets stronger as one approaches the wire. That is also why this effect is the largest for the z-coils, for which the distance in plane between the outermost measuring point and the wire is only about $2.5\,\mathrm{cm}$.

4.3.2 Trapping Region

Since the simulated data resembles the experimental results, the simulation was in turn used to make predictions for the field in the trapping region. Because the actual need for compensation is unknown and can change while the experiment evolves, all pairs were normalized to produce

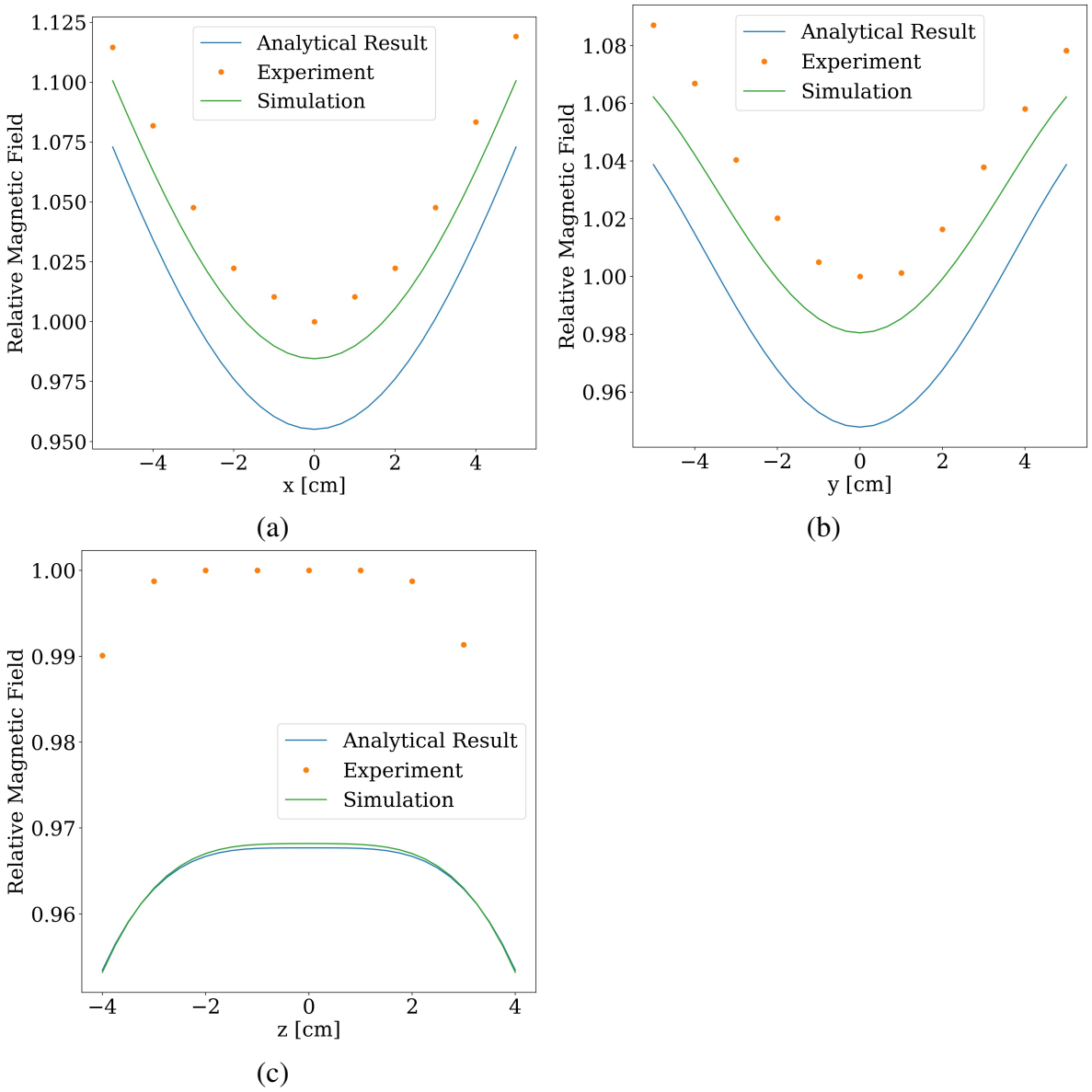

Figure 4.4 Measurement of the component of the magnetic field along the respective common axis of the (a) x-, (b) y- and (c) z-coils and comparison to analytical and simulated results, relative to the center point of the experiment. One can see that for square coils (a and b), the difference between the theory and the simulation is noticeable. Since the simulation takes the shape of the coils into account, its results should be closer to the real field distribution. Also a misalignment can be seen, especially for the z-coils.

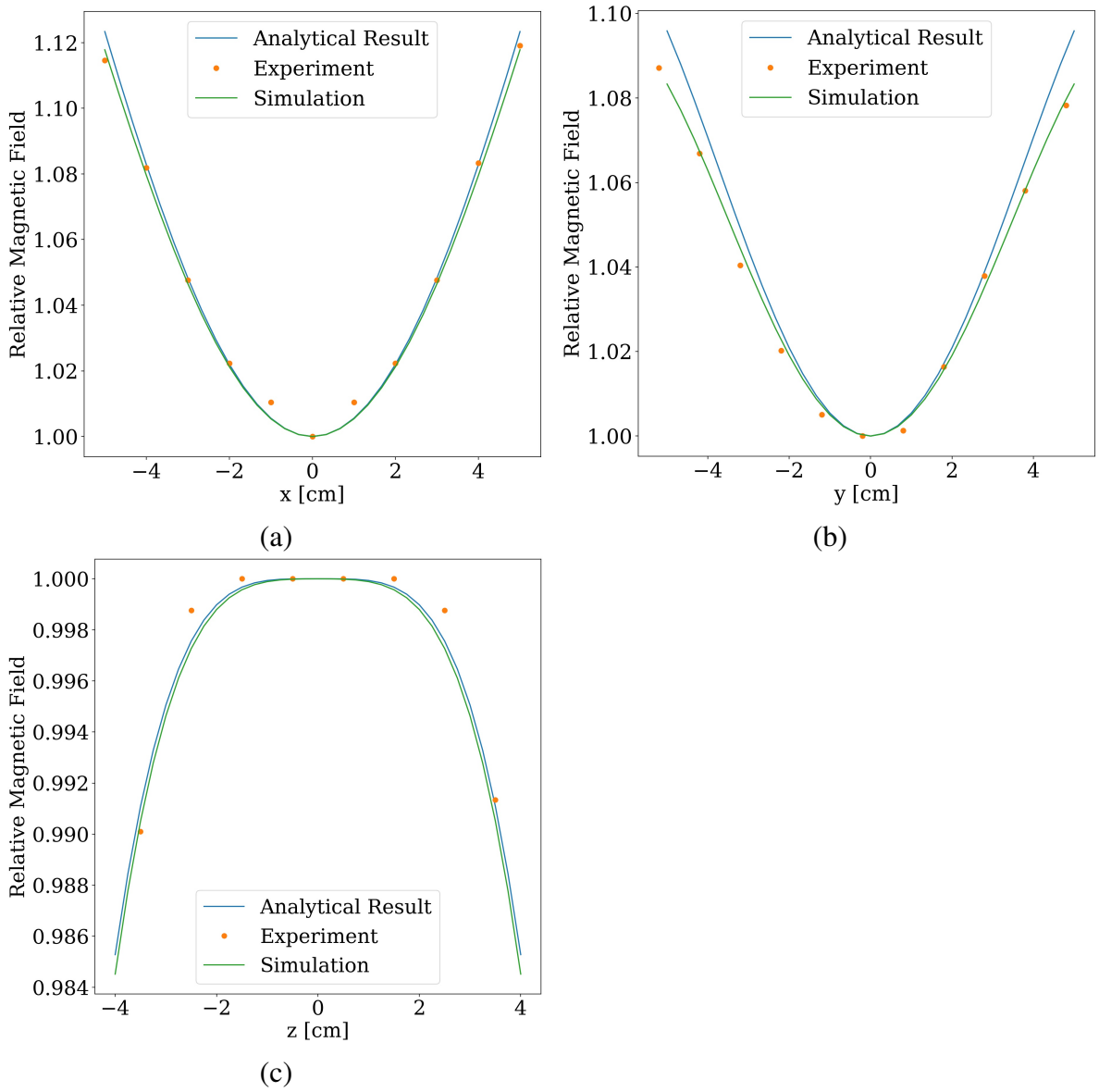

Figure 4.5 Measurement of the component of the magnetic field along the respective common axis of the (a) x-, (b) y- and (c) z-coils and comparison to analytical and simulated results, each being relative to its own center point and with adjusted positions, to visualize differences in shape. Differences between simulation and analytical results are again small. One can be confident, that the shape of the simulated magnetic field resembles the one of the actual coils.

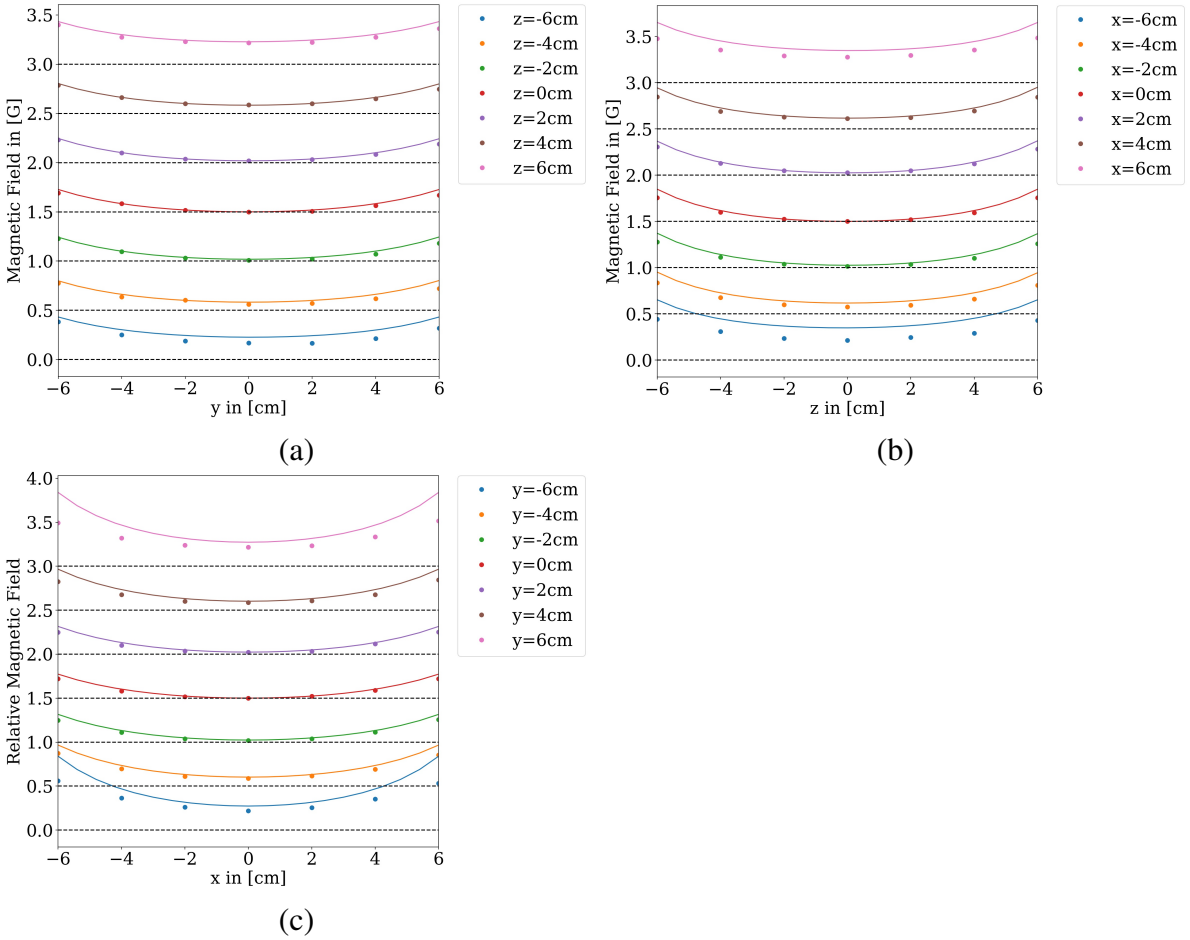

Figure 4.6 Simulation (line) and measurement (points) of the component of the magnetic field, relative to the experimental one at the center, of the (a) x- (b) y and (c) z-coil in their respective planes. For clarity an offset of 0.5 was added between one line and the next, indicated by the black dashed lines, which are the respective zero lines. While there is no notable difference between simulation and experiment at the center points, differences arise close to the edges of the measured region. There the simulated values are all higher than the experimental ones. This is an indication for the magnetic field probe being slightly out of plane.

	x-coil 1 / 2	y-coil 1 / 2	z-coil 1 / 2
B_{theo} [G]	4.81	5.57	5.46
B_{exp} [G]	$4.79/4.80 \pm 0.02$	$5.40/5.45 \pm 0.03$	$5.47/5.44 \pm 0.03$
B_{sim} [G]	4.81	5.57	5.45

Table 4.7 Theoretical, measured and simulated field of the compensation coils in their center for $I = 2\,\text{A}$. Theory and Simulation lead to the same results. This is not surprising since the influence of the shape is minimal at the center point.

the same magnetic field in the center, in the direction of their common axis in the center of the trap. While the actual settings will differ, this can still be used for approximating the influence of nonuniformities induced by the coils. This also yields new values for I/B (which corresponds to IN/B) and therefore (U/B), which should be the most accurate ones in this work and therefore be used for a first setting (see Tab. 4.8).

	x-coil	y-coil	z-coil
$(IN/B)_{\text{theo}}$ [A/G]	23.37	16.65	12.79
$(IN/B)_{\text{sim}}$ [A/G]	22.67 ± 0.02	16.10 ± 0.02	12.79 ± 0.04
$(I/B)_{\text{sim}}$ [mA/G]	453.4 ± 0.5	321.9 ± 0.3	255.7 ± 0.8
$(U/B)_{\text{sim}}$ [mV/G]	983 ± 8	605 ± 5	438 ± 4

Table 4.8 Current and corresponding voltage per Gauss of field in direction of the coil axis in the center of the trap. Errors of the simulated values are explained below.

In addition to the center point the fields absolute values for the whole trapping region got also simulated. Fig. 4.7 shows the results for the plane at $z = 0$ and the edges at $z = \pm 50\,\mu\text{m}$. Although all deviations are on the order of 10^{-7}, the shape at the edges in z-direction reveals that the symmetric center point in these planes is already outside the trapping region. This is inevitable, since this effect is induced by the loss of symmetry, when leaving the shared center point of all three pairs of coils. Only for the center point are the x-, y- and z-component of the field entirely produced by their respective coils. While this does not make a notable difference for deviations this small, especially when compared to the field of the multicoils, it could be noticeable if the coils are not perfectly aligned or are not perfectly shaped like in the simulation. By looking back at Fig. 4.4 one can see that proper alignment is crucial, especially for the x- and y- coils, due to the fact that they are not mounted in Helmholtz-configuration. Although the deviations of the individual components are also small (Fig. 4.8), one can see especially for the z-component, that there are mutual interactions between the compensation coils of different directions. Therefore the uniform area is compressed in one direction and extended in the other one. For the x-, and y-component a similar effect can be seen as a tilt of their axis of symmetry. This is due to the fact that the transverse field component of a coil vanishes on its axis of symmetry only. Perfect alignment on the order of a few micrometer is not possible. Not only would all the center points of the three pairs have to match, they also had to match to the one of the multicoils. And to make matters worse the coils in the simulation are also ideally wound. To estimate these effects one can consider an extended region of 2 cm, for which the trapping region should be within in x- and y-direction. Since

the z-coils are mounted directly on the multicoils and got wound on a form their alignment error should be small. As Fig. 4.9 shows, the single components of the field change by about 10^{-2} within this region. In contrast to the nonuniformities within the trapping region one can level out these offsets by readjusting the currents in the optimization process. The mutual interactions can be seen very well for the z-component in the form of two maxima at the edges, although they are very small in terms of actual rise in field. For the trapping region of $100\,\mu\mathrm{m}$ in one direction the nonuniformities will be smaller than 10^{-3} for the x- and y-direction. Most importantly the z-component, since its direction of the field matches the one of multicoils and therefore adds directly to the absolute field, has nonuniformities on the order of 10^{-4} for the extended region and therefore negligibly small deviations within the trapping region. All in all neither the z-components nor the transverse components nonuniformity should have any major influence on the Feshbach resonance. Therefore the compensation coils can be used to level out undesired magnetic fields without having to worry about any unintentional effects on the scattering lengths.

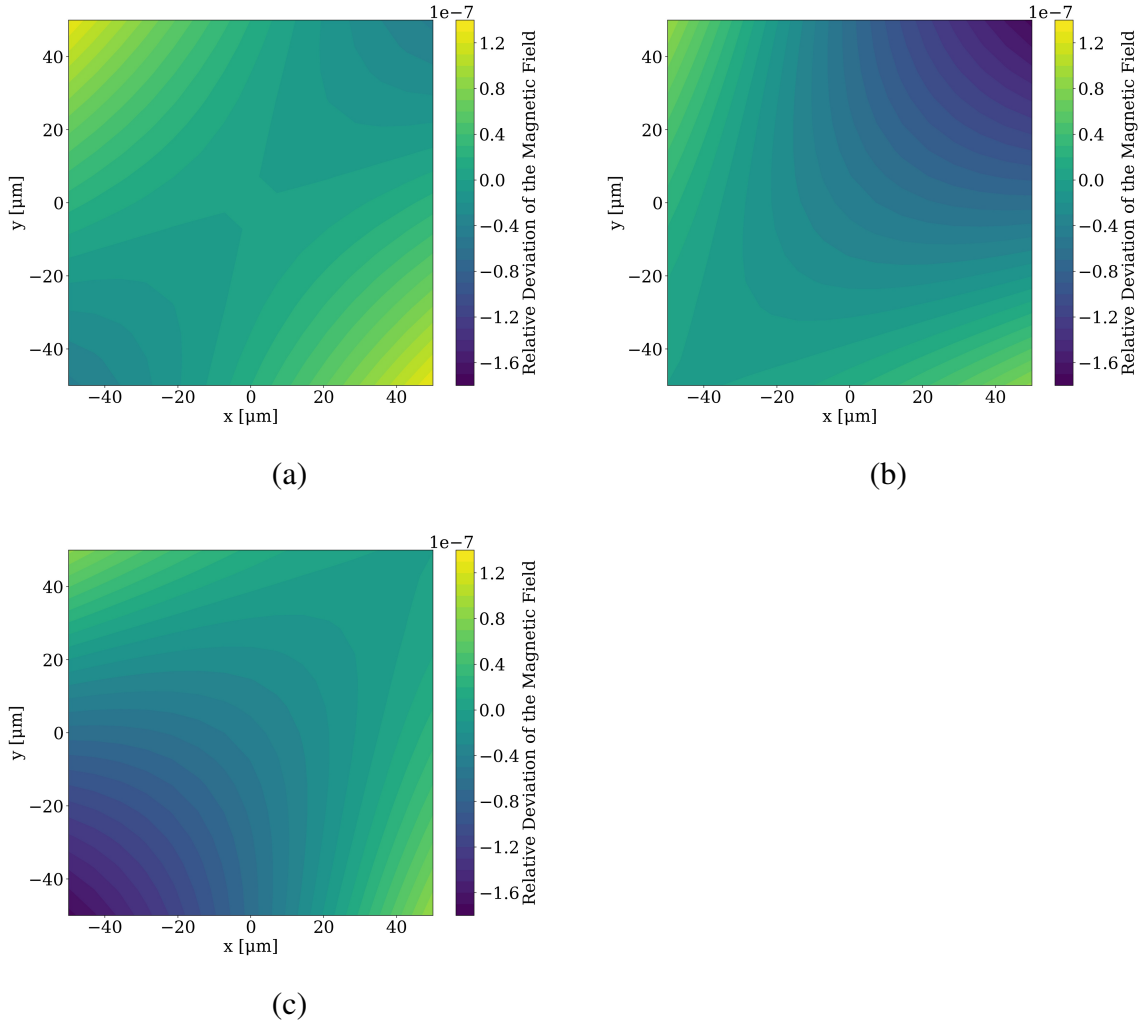

Figure 4.7 Simulation of the deviation of the field relative to the center point of the compensation coils for each pair producing the same absolute field in the center at (a) $z = 0$, (b) $z = 50\,\mu\mathrm{m}$ and (c) $z = -50\,\mu\mathrm{m}$. While the symmetry at the center point in (a) is clearly visible, it gets worse for leaving the plane. This arises from the field components perpendicular to the common axis (which corresponds to the compensating axis) of each pair not vanishing aside this axis of symmetry.

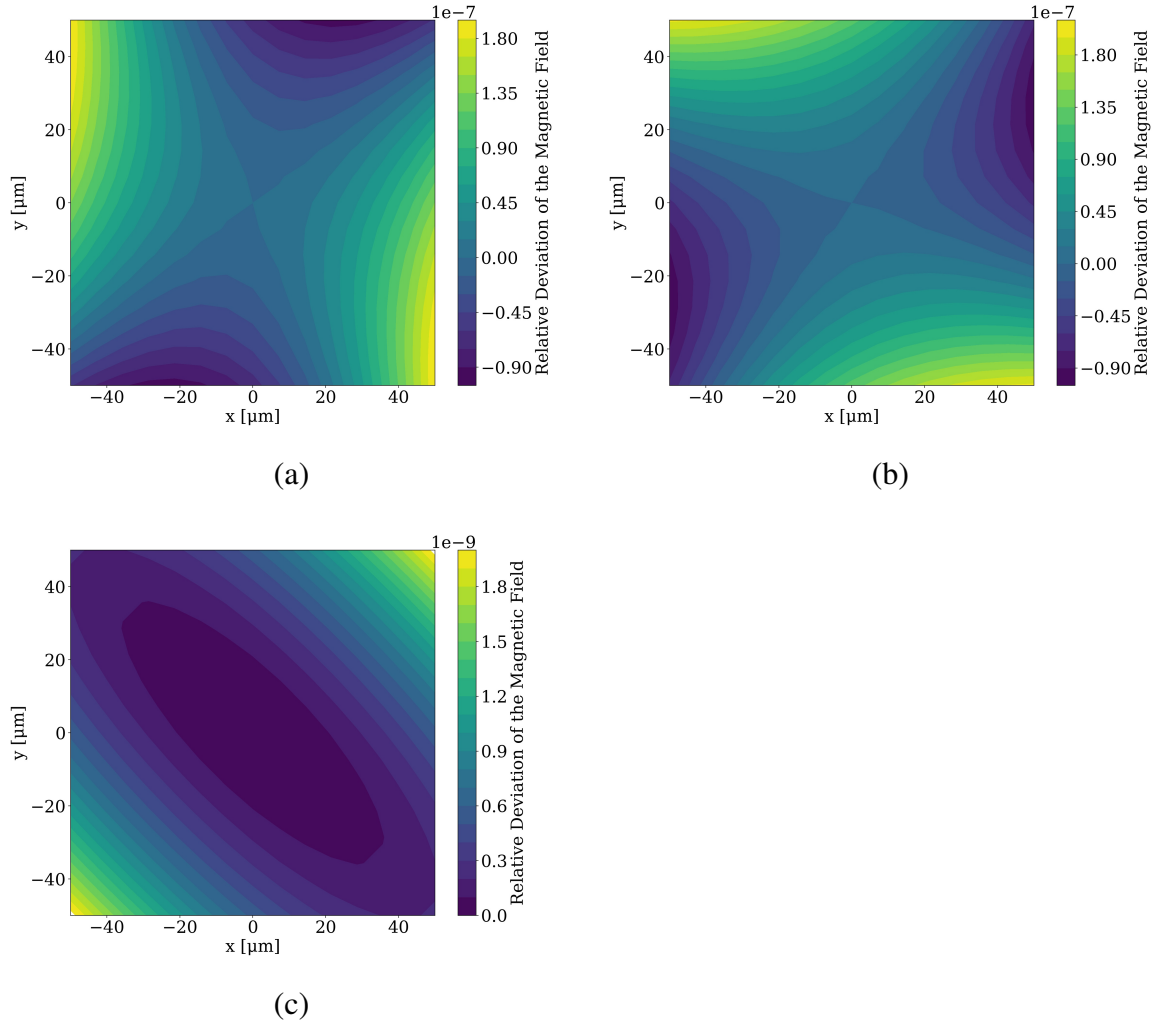

Figure 4.8 Simulation of the (a) x-component, (b) y-component and (c) z-component of the field of the compensation coils for each pair producing equal absolute fields in the center at $z = 0$. For the x- and y- component the mutual interactions between the coils of different directions can be seen in a tilt of the axis of symmetry, whereas for the z-component the region of equal fields gets streched in one and compressed in the other direction.

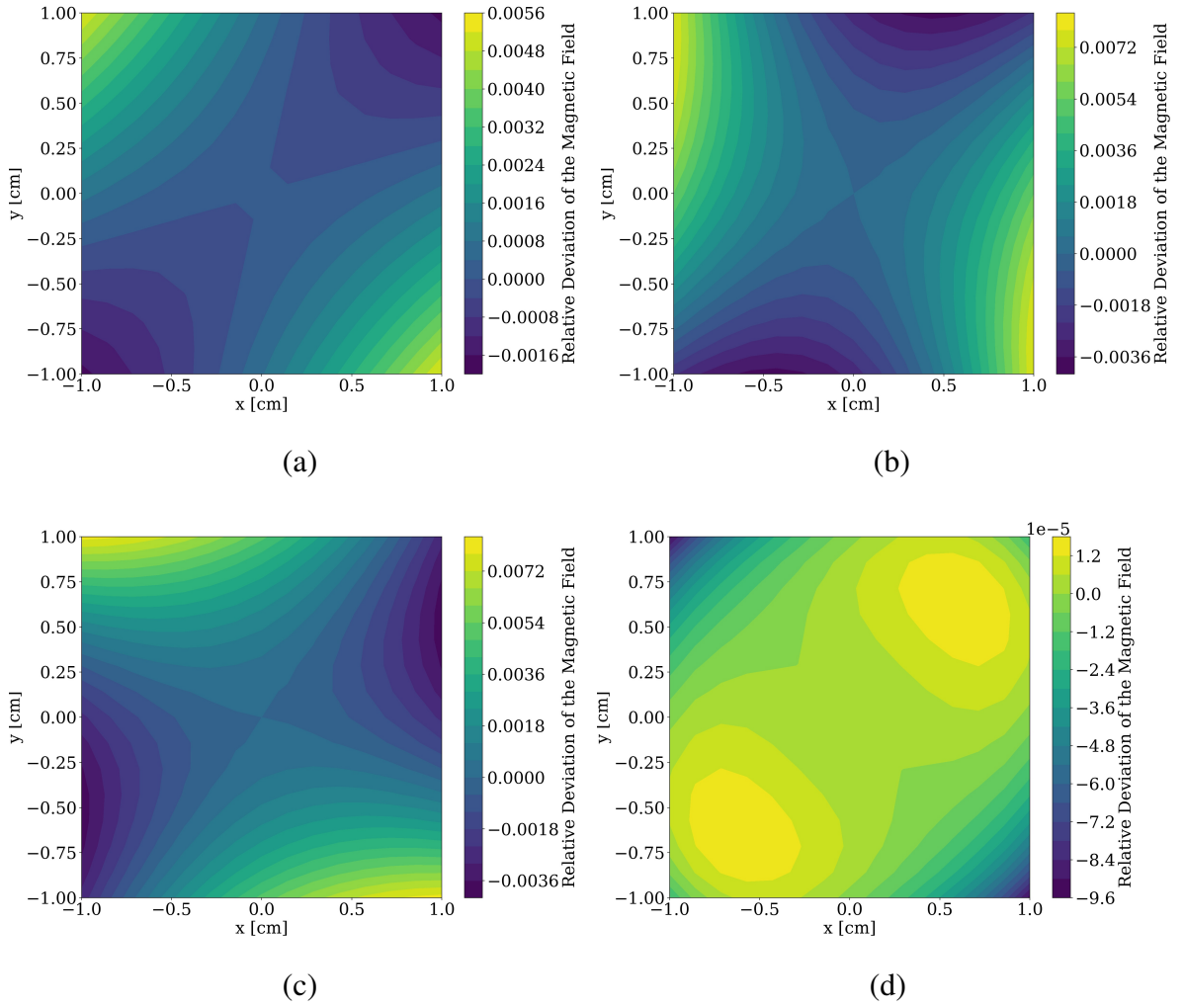

Figure 4.9 Simulation of the (a) absolute value, (b) x-component, (c) y-component and (d) z-component of the field of the compensation coils for each pair producing the same absoulte field in the center at $z = 0$ for an extended region. Compared to Fig. 4.7 and Fig. 4.8, neither the shape of the absolute value of the field, nor the one of the x- and y- component change significantly. By zooming out, two maxima in the z-component became visible, which are a clear sign for the mutual interactions between the fields of the different compensating directions.

5 Conclusion and Outlook

This thesis analyzed the magnetic field properties needed for the preparation of a BEC of ^{39}K with tunable interactions. Water-cooled coils, the so called multicoils are used for the magnetic field gradient of MOT and magnetic trap and to reach the Feshbach resonance of the $|1,1\rangle$ hyperfine state located at (403.4 ± 0.7) G. Since it is not possible to measure the magnetic field of the coils in the trapping region directly, it was simulated instead. A magnetic field of $4.06\,\mathrm{G/A}$ in the center of the Helmholtz configuration and a field gradient of $0.920\,\mathrm{G/(cm\,A)}$ for the z-direction (and about half of this value in perpendicular direction) in the center of the quadrupole configuration were obtained. The simulation also revealed an offset of $475\,\mu\mathrm{m}$ between the center points of the quadrupole configuration and the Helmholtz configuration. It was found that the coils are actually not mounted in Helmholtz configuration, but at a slightly larger distance. The influence of coil imperfections on the fields uniformity and the resulting deviations of the scattering length within the trapping region were investigated.

To compensate effects of any extrinsic fields, pairs of so called compensation coils were designed and built and their magnetic field was both measured and compared to simulated results. With a current of $1\,\mathrm{A}$ in each coil a field of $2.2\,\mathrm{G}$ in x-, $3.1\,\mathrm{G}$ in y- and $3.9\,\mathrm{G}$ in z-direction can be applied. Resistance and inductance of the coils were found to be low enough to avoid excessive heating and allow for fast switching of the fields. The uniformity of the fields was studied for the trapping region as well as for an extended area. Mutual influences of the different compensation directions outside the center were seen in the simulation, but on orders small enough to not significantly influence the behavior of the trap or the scattering lengths on the length scale of the condensate.

While this thesis was written, the 3D-MOT of ^{39}K was achieved, which is one of the big steps towards a successful setup for the planned experiments. The next step will be gray optical molasses for sub-Doppler cooling, which requires the use of the compensation coils to cancel the extrinsic fields. As soon as atoms are loaded into the optical dipole trap, the Feshbach resonance at $403.4\,\mathrm{G}$ will be used to enhance the evaporation process and to tune to positive scattering lengths, which is a prerequisite for successful Bose-Einstein condensation. After a BEC is produced, RF-spectroscopy can be performed, which gives precise access to the field distribution within the trapping region.

Based on this thesis, one can be quite confident, that the magnetic field setup is well suited to reach a ^{39}K BEC with precisely tunable interactions.

6 Appendix

A Code

Function for evaluation of the magnetic field in python:

```
@jit
def B_field(r,I,r_0):
 v = 0
 for i in range(len(r)-1):
  dl = r[i+1]-r[i]
  v = v + (np.cross(dl,r[i]-r_0)/(sum((r[i]-r_0)**2)**(3/2)))
 B = 0.1*I*v
return B
```

The function takes the list of points from Engauge Digitizer r, the current I and the point at which the field is calculated r_0. @jit is needed to use the numba package, which speeds up the evaluation.

B Resolution of the Magnetic Field Simulation

The number of operations scales not only with number of points the field gets calculated for, which goes already quadratic for the two-dimensional grids, but of course also with the chosen resolution of the coils. Due to limited computing power one therefore has to make a trade-off between accuracy of single results and grain size of the grid or chain. In Figs. B.1 and B.2 one can see the results for the coil axis of the z- and y-direction, which represent a circular and rectangular coil, for different resolutions. As one can see in both cases, the results converge quite fast. Therefore the highest resolution of 2000 points per turn can be assumed to be exact and one can calculate errors based on that. For resolutions higher than 80 points per turn the relative error is already smaller than 10^{-3} and nearly constant. This means that the overall shape remains unaffected by the resolution, which is great for the accuracy of the derived results for the trapping region. Since the multicoils got simulated with over 200 points per turn, one can be quite confident about the accuracy of their simulation as well.

To understand the errors one has to look at the changes, which arise by increasing the resolution. If the wire element is divided in multiple smaller ones before evaluating, the absolute distance gets more precise in the case of the square coils, since it is always taken to the starting point of the element but in reality changes within. Also the angles precision increases. In the case of the square coil the angles precision does not affect the total values of the cross products, since these are always twice the area of the spanned triangle, which is when summed up over one side the total area of the triangle spanned by the side and the point, the field is evaluated for. Also the resulting field direction is unaffected, because it is always perpendicular to the spanned triangle. This means the error for square coils consists entirely of the precision of the weighting of these crossproducts by the distance. For circular coils one gets a somewhat opposite picture. This time the distances are correct as long as one calculates for points on the axis of symmetry, since the starting points of the wire elements are always on the circle and the distance to the wire does not change. Instead the total values of the crossproducts change. This can be understood easily by considering the center point of the plane. Here the sum over all crossproducts yields twice the area of the polygon, which approximates the circle. ‘poly’ represents the resolution of the wireloop and it is clear that this area converges to $2\pi R^2$ for high resolution, while the sum over all wire elements goes to $2\pi R$, which is the real length of the wire. When one goes out of plane, the area becomes the surface of a cone. Then the direction of the normal vector changes, while going around the cone. This means that the direction of the resulting field changes with the resolution. While being on the axis of symmetry this effect levels out for summing over all directions, since the distances which determine the weights of the sum are exact. Aside the axis of symmetry this is not the case, but this relative distance errors vanish pretty fast with increasing resolution and distance to the wire.

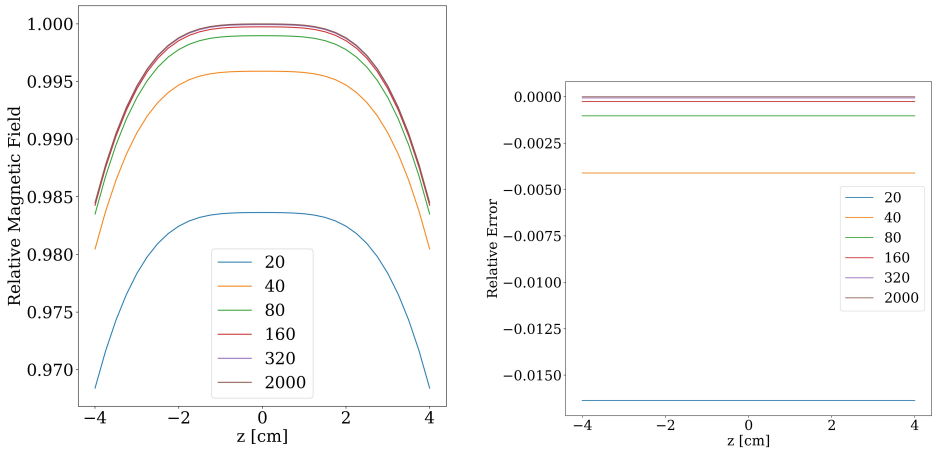

(a) (b)

Figure B.1 Simulation of the magnetic field along z-axis relative to the center point for different resolutions (a) and relative deviation from highest resolution (b) for a pair of circular coils. The results in (a) converge quite fast. Although the highest resolution of 2000 points per turn is significantly higher than all the others, the difference in resulting field can hardly be seen. The relative differences to the highest resolution are nearly constant. This means the shape is nearly unaffected by the resolution.

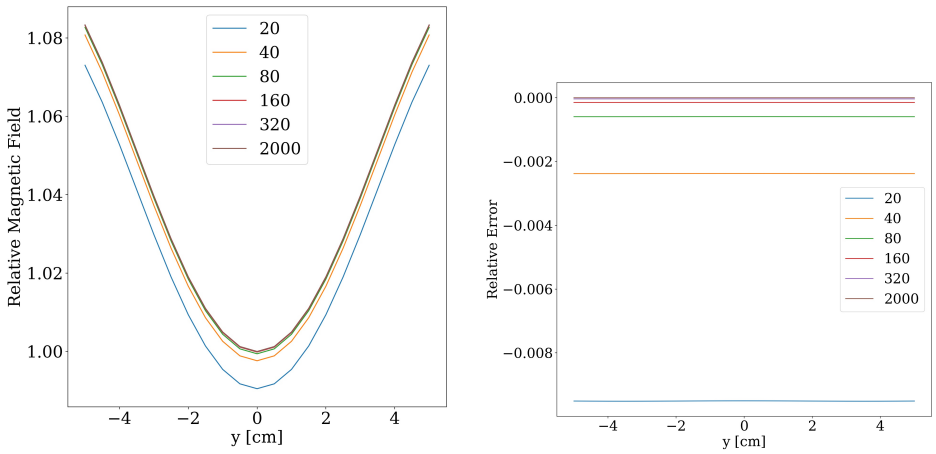

(a) (b)

Figure B.2 Simulation of the magnetic field along y-axis relative to the center point for different resolutions (a) and relative deviation from highest resolution (b) for a pair of square coils. Although the range of the relative magnetic field axis is higher and therefore increases this effect, the results seem to converge even faster than for the circular coils (see B.1). This is confirmed by the relative error which is almost halved and also nearly constant. Errors for square coils consist entirely of the error of the distance to the wire, since it is taken to the starting point of the wire element but changes within. The fact that the sum over the cross products is independent of the resolution, seems to let the total results converge faster.

C Lists

List of Figures

List of Tables

Bibliography

[1] A. Einstein. *Quantentheorie des einatomigen idealen Gases.* Sitzungsberichte der Preussischen Akademie der Wissenschaften , 261–267 (1924).

[2] A. Einstein. *Quantentheorie des einatomigen idealen Gases: Zweite Abhandlung.* Sitzungsberichte der Preussischen Akademie der Wissenschaften , 3–14 (1925).

[3] M. Anderson, J. Ensher, M. Matthews, C. Wieman, and E. Cornell. *Observation of Bose-Einstein Condensation in a Dilute Atomic Vapor.* Science **269**, 198–201 (1995).

[4] K. B. Davis, M.-O. Mewes, M. R. Andrews, N. J. van Druten, D. M. K. D. S. Durfee, and W. Ketterle. *Bose-Einstein Condensation in a Gas of Sodium Atoms.* Phys. Rev. Lett. **75**, 3969–3973 (1995).

[5] R. P. Feynman. *Simulating physics with computers.* International Journal of Theoretical Physics **21**, 467–488 (1982).

[6] C. D'Errico, M. Zaccanti, M. Fattori, G. Roati, M. Inguscio, G. Modugno, and A. Simoni. *Feshbach resonances in ultracold 39K.* New Journal of Physics **9**, 223 (2007).

[7] M. Landini, S. Roy, G. Roati, A. Simoni, M. Inguscio, G. Modugno, and M. Fattori. *Direct evaporative cooling of 39K atoms to Bose-Einstein condensation.* Phys. Rev. A **86**, 033421 (2012).

[8] G. Salomon, L. Fouché, P. Wang, A. Aspect, P. Bouyer, and T. Bourdel. *Gray-molasses cooling of 39 K to a high phase-space density.* Europhysics Letters **104**, 63002 (2013).

[9] R. Grimm, M. Weidemüller, and Y. B. Ovchinnikov. *Optical dipole traps for neutral atoms.* Advances In Atomic, Molecular, and Optical Physics **42**, 95–170 (2000).

[10] C. Dornes. *3D-focusing Spectrometer for a Reaction Microscope*. Master's thesis. Heidelberg University (2011).

[11] T. Tiecke. *Feshbach resonances in ultracold mixtures of the fermionic quantum gases 6Li and 40K*. Ph.D. thesis. University of Amsterdam (2009).

[12] C. J. Foot. *Atomphysik* (Oldenbourg-Verl., München, 2011) pp. XV, 428 S.

[13] A. Bambini and A. Agresti. *Radiative cooling force in atoms with multiplet structure.* Phys. Rev. A **56**, 3040–3055 (1997).

[14] W. H. Wing. *On neutral particle trapping in quasistatic electromagnetic fields.* Progress in Quantum Electronics **8**, 181–199 (1984).

[15] D. Nath, R. K. Easwaran, G. Rajalakshmi, and C. Unnikrishnan. *Accelerated Thermalisation of 39K atoms in a Magnetic Trap with Superimposed Optical Potential.* Journal of Physics B **46**, 155303 (2013).

[16] D.M.Brink and C.V.Sukumar. *Majorana spin-flip transitions in a magnetic trap.* Phys. Rev. A **74**, 035401 (2006).

[17] J. L. Roberts, N. R. Claussen, S. L. Cornish, E. A. Donley, E. A. Cornell, and C. E. Wieman. *Controlled Collapse of a Bose-Einstein Condensate.* Phys. Rev. Lett. **86**, 4211–4214 (2001).

[18] G. Roati, M. Zaccanti, C. D'Errico, J. Catani, M. Modugno, A. Simoni, M. Inguscio, and G. Modugno. *39-K Bose-Einstein condensate with tunable interactions.* Phys. Rev. Lett. **99**, 010403 (2007).

[19] C. Pethick and H. Smith. *Bose-Einstein condensation in dilute gases*. 2nd ed. (Cambridge University Press, Cambridge, 2008).

[20] T. Schuster. *Feshbach resonances and periodic potentials in ultracold Bose-Fermi mixtures*. Ph.D. thesis. Heidelberg, University. (2012).

[21] M. E. Rudd and J. R. Craig. *Optimum Spacing of Square and Circular Coil Pairs.* Review of Scientific Instruments **39**, 1372–1374 (1968).

[22] F. W. Grover. *Formulas and tables for the calculation of the inductance of coils of polygonal form.* Scientific Papers of the Bureau of Standards **18**, 737–762 (1922).

[23] J. D. Jackson. *Classical electrodynamics*. 3rd ed. (Wiley, New York, 1999).

[24] M. Mitchell, B. Muftakhidinov, and T. W. et al. *Engauge Digitizer Software.* Last Accessed: August 16, 2017.

Danksagung

An dieser Stelle möchte ich allen danken, die mich während der vergangenen fünf Monate unterstützt, und damit zum Gelingen dieser Arbeit beigetragen haben.

- Zuerst möchte ich Prof. Markus K. Oberthaler danken, der mich in seiner Gruppe aufgenommen und damit diese Arbeit und die Zeit am BECK erst ermöglicht hat. Er war immer optimistisch, was die Fortschritte am Experiment angeht und hat mit seiner Begeisterung für Physik immer wieder angesteckt.
- Ebenso möchte mich bei Prof. Selim Jochim bedanken, der sich als Zweitkorrektor zur Verfügung gestellt hat.
- Ganz besonders möchte ich mich bei Helmut Strobel für die intensive Betreuung dieser Arbeit bedanken. Während meiner Zeit am BECK hat er mir unzählige Fragen beantwortet und mich so von seiner Expertise profitieren lassen. Außerdem stammt von ihm und Maurus die Idee, die Multicoils zu scannen, was den Grundstein für diese Arbeit gelegt hat.
- Daher gilt mein Dank auch Maurus Hans, der außerdem mit Diskussionen und Anregungen rund um die Simulation geholfen hat und viel Zeit in der Werkstatt verbracht hat, um Spulenwickeltools herzustellen.
- Celia Viermann möchte ich ebenfalls danken. Sie half mir bei den ersten Versuchen runde Spulen zu wickeln und stand immer für Fragen zur Verfügung.
- Dem anderen Bachelorstudenten am BECK, Alexander Impertro, danke ich für viele gute Diskussionen und die gemeinsame Zeit am Experiment.
- Ich danke auch den BEClern aus meinem Büro, von denen immer jemand für Fragen zur Verfügung stand. Außerdem ermöglichten sie viele gute Gespräche und Diskussionen, nicht nur fachlicher Natur.
- Der ganzen übrigen Matterwave-Gruppe danke ich für die gute Zeit, das Frühstück am Freitag morgen, sowie eine Vielzahl kleinerer Hilfen und guter Gespräche.
- Zuletzt bedanke ich mich bei meinen Eltern, von denen die naturwissenschaftliche Prägung stammt, sowie meinen Freunden, die mich alle während des gesamten Bachelorstudiums begleitet und unterstützt haben.

Erklärung

Ich versichere, dass ich diese Arbeit selbstständig verfasst und keine anderen als die angegebenen Quellen und Hilfsmittel benutzt habe.

Heidelberg, den 22.08.2017,